A Reduced Order Model of Two-Phase Flow, Heat Transfer and Combustion in Circulating Fluidized-Beds

Final Report
Reporting Period Start Date: 10/01/00
Reporting Period End Date: 9/30/03
Principal Investigator: Paul Cizmas
Date Report was Issued: December 2003

DOE Award Number: DE-FC26-00NT40903

Texas Engineering Experiment Station
Office of Sponsored Research
332 Wisenbaker Engineering Research Center, 3000 TAMU
College Station, TX 77843-3000

and

Antonio Palacios
San Diego State University
San Diego, CA 92182-7720

Disclaimer

This report was prepared as an account of work sponsored by an agency of the United States Government. Neither the United States Government nor any agency thereof, nor any of their employees, makes any warranty, express or implied, or assumes any legal liability or responsibility for the accuracy, completeness, or usefulness of any information, apparatus, product, or process disclosed, or represents that its use would not infringe privately owned rights. Reference herein to any specific commercial product, process, or service by trade name, trademark, manufacturer, or otherwise does not necessarily constitute or imply its endorsement, recommendation, or favoring by the United States Government or any agency thereof. The views and opinions of authors expressed herein do not necessarily state or reflect those of the United States Government or any agency thereof.

Abstract

The report summarizes the objectives, tasks and accomplishments of this research project. The report presents the following program deliverables: (1) database generation using MFIX code, (2) development and implementation of an algorithm to calculate the proper orthogonal decomposition (POD) basis functions, (3) visualization tools for reconstructing simulated data, (4) algorithms for reducing the partial differential equations to ordinary differential equations, (5) visualization tools for Galerkin ordinary differential equations, (6) verification and validation of the code by comparing POD and conventional solution results, and (7) development of POD strategy for best energy cut-off values.

Contents

1 Introduction **8**

2 Executive Summary **9**

3 Experimental **10**

4 Results and Discussion **10**
4.1 Database generation using the MFIX code 10
4.2 Algorithm for POD basis functions calculation 10
4.3 Visualization tools for the reconstruction of simulated data 25
4.4 Algorithm for reducing partial differential equations to ordinary differential equations 25
4.4.1 Reduced order model based on proper orthogonal decomposition for gas-only flows 26
4.4.1.1 ODExMFIX 27
4.4.1.2 ODEx3 29
4.4.1.3 Results for compressible, gas-only flows 36
4.4.1.3.1 Results at reference condition 40
4.4.1.3.2 Results at off-reference conditions 48
4.4.2 Reduced order model based on proper orthogonal decomposition for gas-solids transport phenomena 50
4.4.2.1 Results for gas-solids transport phenomena in a fluidized bed 54
4.4.2.1.1 Results at reference condition 57
4.4.2.1.2 Results at off-reference conditions 57
4.5 Visualization tools for Galerkin ODEs 67

5 Conclusions **67**

A SAMPLE INPUT FILE FOR ODExMFIX **69**

B SAMPLE INPUT FILE FOR ODEx3 **70**

C SAMPLE INPUT FILE FOR ODExS **71**

List of Figures

1 Case I. Snapshots of ϵ_g. 10
2 Case I. Snapshots of V_g. 11
3 Case II. Snapshots of ϵ_g. 11
4 Case II. Snapshots of V_g. 12
5 Case I. POD modes of ϵ_g 12
6 Case I. POD energy spectrum of ϵ_g. 13
7 Case I. POD time series of ϵ_g. 14
8 Case I. POD phase-space projections of ϵ_g. 15
9 Case I. POD modes of V_g 16
10 Case I. POD energy spectrum of V_g. 16
11 Case I. POD time series of V_g. 17
12 Case I. POD phase-space projections of V_g. 18
13 Case II. POD modes of ϵ_g 19
14 Case II. POD energy spectrum of ϵ_g. 19
15 Case II. POD time series of ϵ_g. 20
16 Case II. POD phase-space projections of ϵ_g. 21
17 Case II. POD modes of V_g 22
18 Case II. POD energy spectrum of V_g. 22
19 Case II. POD time series of V_g. 23
20 Case II. POD phase-space projections of V_g. 24
21 Control volume for mass balance 28
22 Control volume for momentum balance 32
23 Case G: geometry, boundary conditions, and computational grid 36
24 Case G: the first six basis functions of u 37
25 Case G: the first six basis functions of v 37
26 Case G: the first six basis functions of p 38
27 Case G: cumulative energy 39
28 Case G: the first four time coefficients of v 41
29 Case G: the first four time coefficients of u 42
30 Case G: the first four time coefficients of p 43
31 Case G: α_1^p predicted by ODExMFIX using two sets of snapshots 44
32 Case G: contour plots of velocity u predicted with MFIX and ODExMFIX 45
33 Case G: contour plots of velocity v predicted with MFIX and ODExMFIX 46
34 Case G: contour plots of pressure p predicted with MFIX and ODExMFIX 47
35 Case G: errors ϵ_u and ϵ_v at time t=13 s for different values of viscosity 49
36 Case G: errors ϵ_u at three time values and for different values of viscosity 50
37 Case G: errors ϵ_v at three time values and for different values of viscosity 50
38 Case G: contour plots of velocity u_g at different values of viscosity 51
39 Case G: contour plots of velocity v_g at different values of viscosity 51
40 Case I: geometry, boundary conditions, and computational grid 54
41 Case I: the first six basis functions of p_g 55
42 Case I: the first six basis functions of u_g 56
43 Case I: the first six basis functions of v_g 56

44 Case I: the first six basis functions of u_s 56
45 Case I: the first six basis functions of v_s 57
46 Case I: the first four time coefficients of u_g obtained from ODExS 58
47 Case I: the first four time coefficients of v_g obtained from ODExS 59
48 Case I: the first four time coefficients of u_s obtained from ODExS 60
49 Case I: the first four time coefficients of v_s obtained from ODExS 61
50 Case I: ϵ_g at $t = 1s$ 62
51 Case I: p_g at $t = 1s$ 62
52 Case I: u_g at $t = 1s$ 63
53 Case I: v_g at $t = 1s$ 63
54 Case I: u_s at $t = 1s$ 64
55 Case I: v_s at $t = 1s$ 64
56 Case I: ODExS errors at off-reference conditions 66
57 Case I: contour plots of ϵ_g at $t = 1s$ and different D_p 67

List of Tables

1 Values of left-hand-side and right-hand-side terms of the x-momentum conservation equation at different grid locations in MFIX and in the reduced order model. 26
2 Reduced order models for gas-only flows 27
3 Parameters of case G 37
4 Case G: errors of ODExMFIX at different values of μ_0 48
5 Parameters of case I 55
6 Case I: POD energy vs number of modes for p_g, u_g, v_g, u_s, and v_s 55
7 Case I: ODExS errors at reference condition 57
8 Case I: ODExS errors at off-reference conditions 65

1 Introduction

The report presents the research activity completed during this project. The report describes the tasks assigned, the accomplishments and challenges, as well as the results obtained. The section Results and Discussion briefly presents the research objectives of the project and describes how these tasks were accomplished. This section also presents a sample of the results obtained. There were no changes in the approach originally proposed to complete the research program, although additional methodologies have been explored in order to implement the algorithm for reducing the partial differential equations (PDEs) to ordinary differential equations (ODEs).

2 Executive Summary

The modeling of dense multiphase flow reactors is crucial for circulating fluidized-bed combustors and fluid catalytic cracking risers. The governing equations describing the phenomena inside multiphase flow reactors consist of a system of highly coupled partial differential equations. Solving these equations is a difficult and computing intensive task. One of the goals of this project is to reduce the computational effort by developing a reduced order model based on the proper orthogonal decomposition (POD) method. Another goal of this project is to develop a visualization package for the analysis of transport phenomena, as well as for the storage of the information produced by numerical simulation and/or experimental investigation.

The report presents the research activity completed during this project. The report describes the tasks assigned, the accomplishments and challenges, as well as the results obtained. The goals of the project were to (1) generate database generation using MFIX code, (2) develop and implement an algorithm to calculate POD basis functions, (3) develop visualization tools for reconstructing simulated data, (4) develop algorithms for reducing the partial differential equations to ordinary differential equations, (5) develop visualization tools for Galerkin ordinary differential equations, (6) verify and validate the code by comparing POD and conventional solution results, and (7) develop of POD strategy for best energy cut-off values.

The first two tasks, the database generation, and the development and implementation of an algorithm to calculate POD basis functions have been completed in the first year of the project. The third task, the development of visualization tools for reconstructing simulated data, included visualization of reconstructed flow motion, and visualization of flow motion in phase space through POD time coefficients. Using POD spatial modes, visualizations of the reconstructed flow motion were generated. POD amplitude coefficients were used to create animations of the temporal behavior of the flow in phase space.

The fourth task, the development of an algorithm for reducing the partial differential equations (PDEs) to ordinary differential equations (ODEs), generated several implementations of the reduced order models. The main implementations included: (1) ODEx and ODEx3, reduced order models that followed MFIX discretization, although required reorganization of the discretized equations before projection on the basis functions; (2) ODExNL, a reduced order model implementation similar to ODEx, in which the system of ODEs has been transformed into a non-linear system of equations; (3) ODExMIN, a reduced order model implementation in which instead of projecting the PDEs on the basis functions, the time coefficients were solved using an error minimization methodology; (4) ODExMFIX, a reduced order model in which the implementation closely followed the MFIX code; and (5) ODExS, a hybrid reduced order model that did not reduce the order of the solids volume fraction correction equation.

The fifth task, the development of visualization tools for Galerkin ODEs, included visualization of reconstructed flow motion, and visualization of flow motion in phase space through POD time coefficients. Using POD spatial modes, visualizations of the reconstructed flow motion were generated. POD amplitude coefficients were used to create animations of the temporal behavior of the flow in phase space. The sixth task, verification and validation of the POD results, has been completed for several cases. A strategy for defining the energy cut-off value has been implemented.

3 Experimental

No experimental work has been planned or completed during this reporting period.

4 Results and Discussion

This section presents the results obtained during the project. The results are grouped according the program deliverables.

4.1 Database generation using the MFIX code

Two cases have been simulated in order to verify that the MFIX code has been properly installed. The input data for these cases has been provided by NETL. Case I consisted of the flow in a fluidized bed with a jet, as described in [2], p. 156. Case I was run to simulate the flow for 5 seconds. The results of Case I was validated using the animation provided by NETL. Figures 1 and 2 show two representative examples of the simulations. In particular, Figure 1 illustrates the variations in void fraction, while Figure 2 illustrates the variations in the y-component of gas velocity.

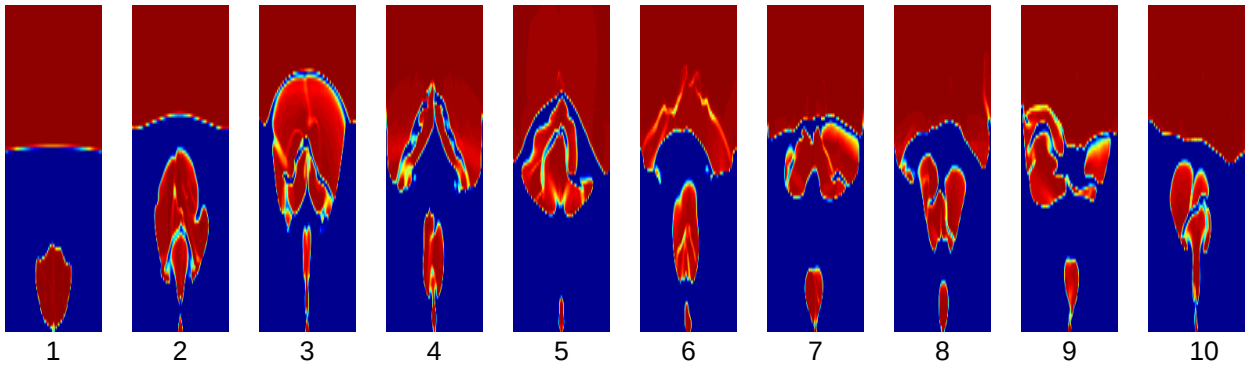


Figure 1: Case I. Snapshots of ϵ_g.

Case II consisted of the flow in the bubbling fluidized bed as described in the ORNL experiments. Case II included two sub-cases, corresponding to two different values of y-component of the gas velocity, V_g. In case II.1 the velocity was V_g=12.6 while in case II.2 the velocity was V_g=16.8. Thus, in case II.1, the simulations are near the bifurcation point where the bubbles appear. Case II.2 is far away from the bifurcation point so that the bubble dynamics is more disorganized. As a result, a more coherent behavior is observed in case II.1 than in case II.2. The snapshots of the packed bed void fraction, ϵ_g, and the velocity V_g are shown in Figs. 3 and 4.

4.2 Algorithm for POD basis functions calculation

An algorithm for calculating the POD basis functions has been implemented. This algorithm has been tested for case I presented in the previous section. Figures 5-8 show the POD analysis of the void fraction variable, ϵ_g. The zeroth POD mode, which is also the time average of the simulations, reflects the left-to-right symmetry of the fluidized bed. The remaining modes describe principal

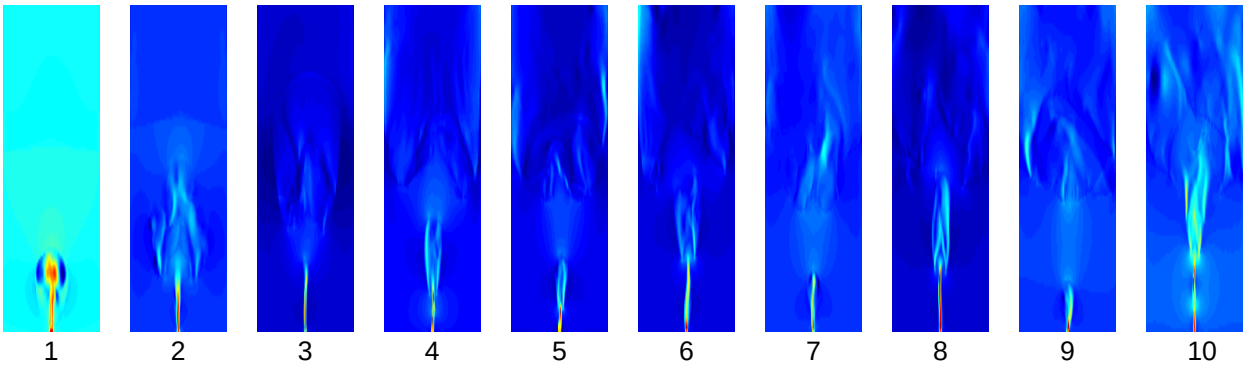


Figure 2: Case I. Snapshots of V_g.

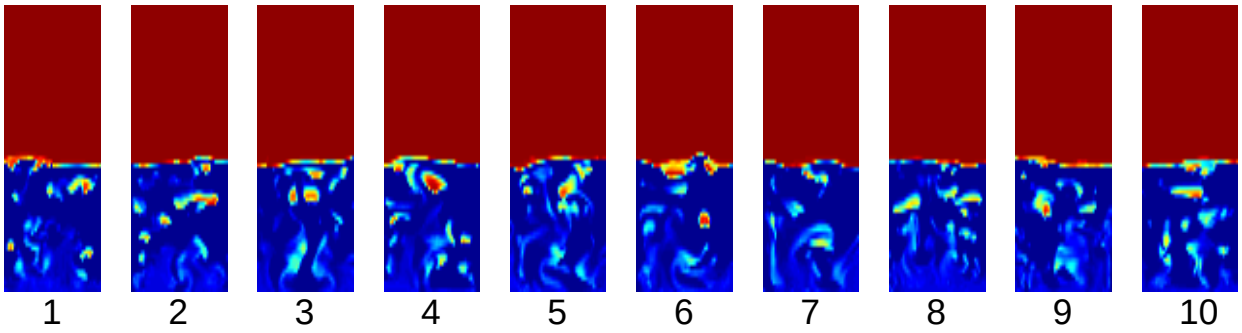


Figure 3: Case II. Snapshots of ϵ_g.

coherent structures in the evolution of the flow. The times series and phase-space projections of the corresponding amplitude coefficients further illustrate the periodic nature of the flow. Similarly, Figs. 9-12 describe the results of the POD analysis of the y-component of the gas velocity, V_g. For both variables, ϵ_g and V_g, the POD energy spectrum provides an estimate for the dimensionality of the problem and consequently, the number of equations that might be required in the reduction from a partial differential equations model to a reduced model based on ordinary differential equations.

Results of the POD analysis for case II are shown in Figs. 13-20. Additional results have been presented in [1]. The algorithm for performing the POD decomposition was also tested on a complex flow with large unsteadiness, such as the flow in turbomachinery cascades. A detailed analysis had been done in this case to evaluate the influence of the energy cut-off value on the solution reconstruction.

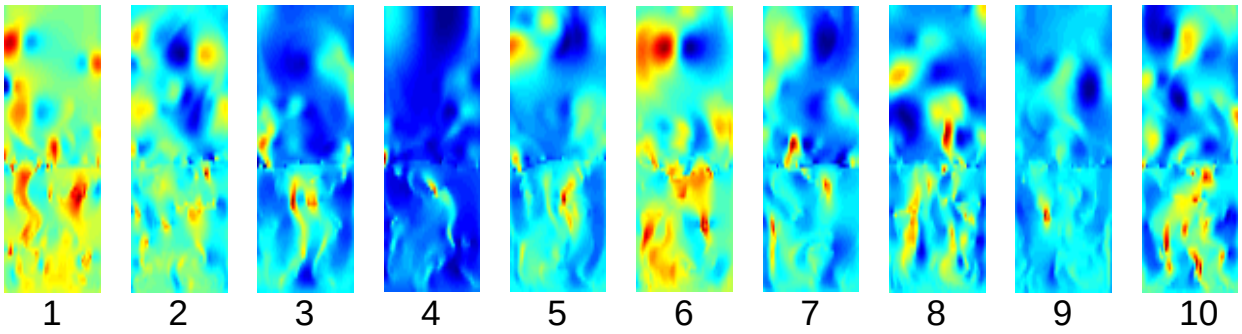


Figure 4: Case II. Snapshots of V_g.

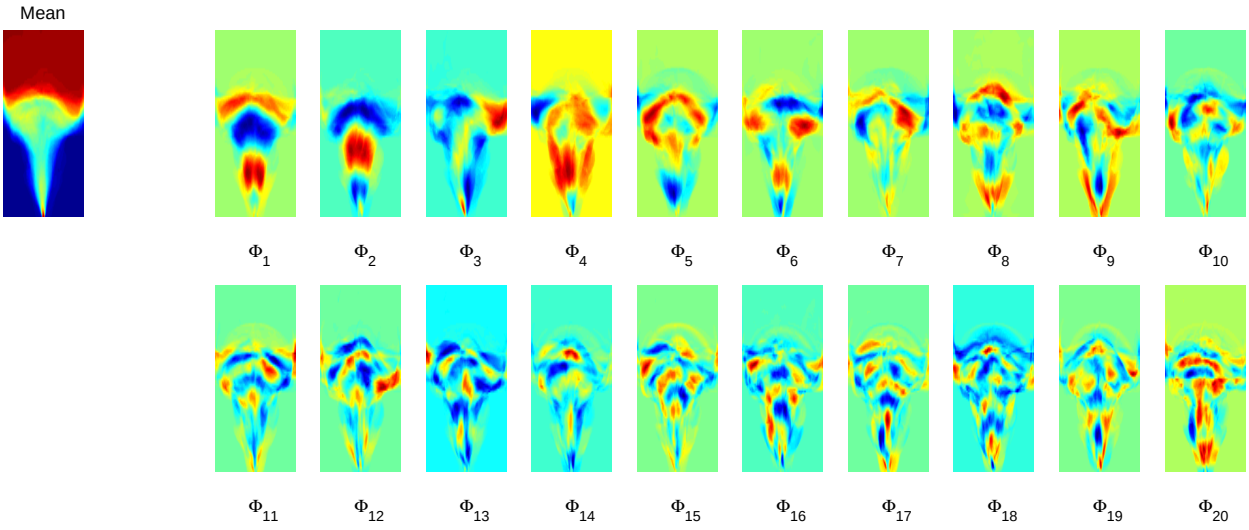


Figure 5: Case I. POD modes of ϵ_g

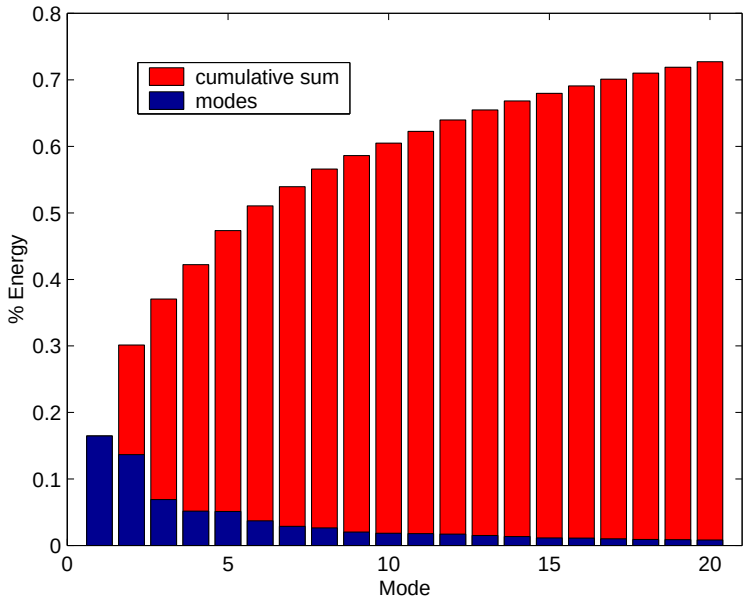


Figure 6: Case I. POD energy spectrum of ϵ_g.

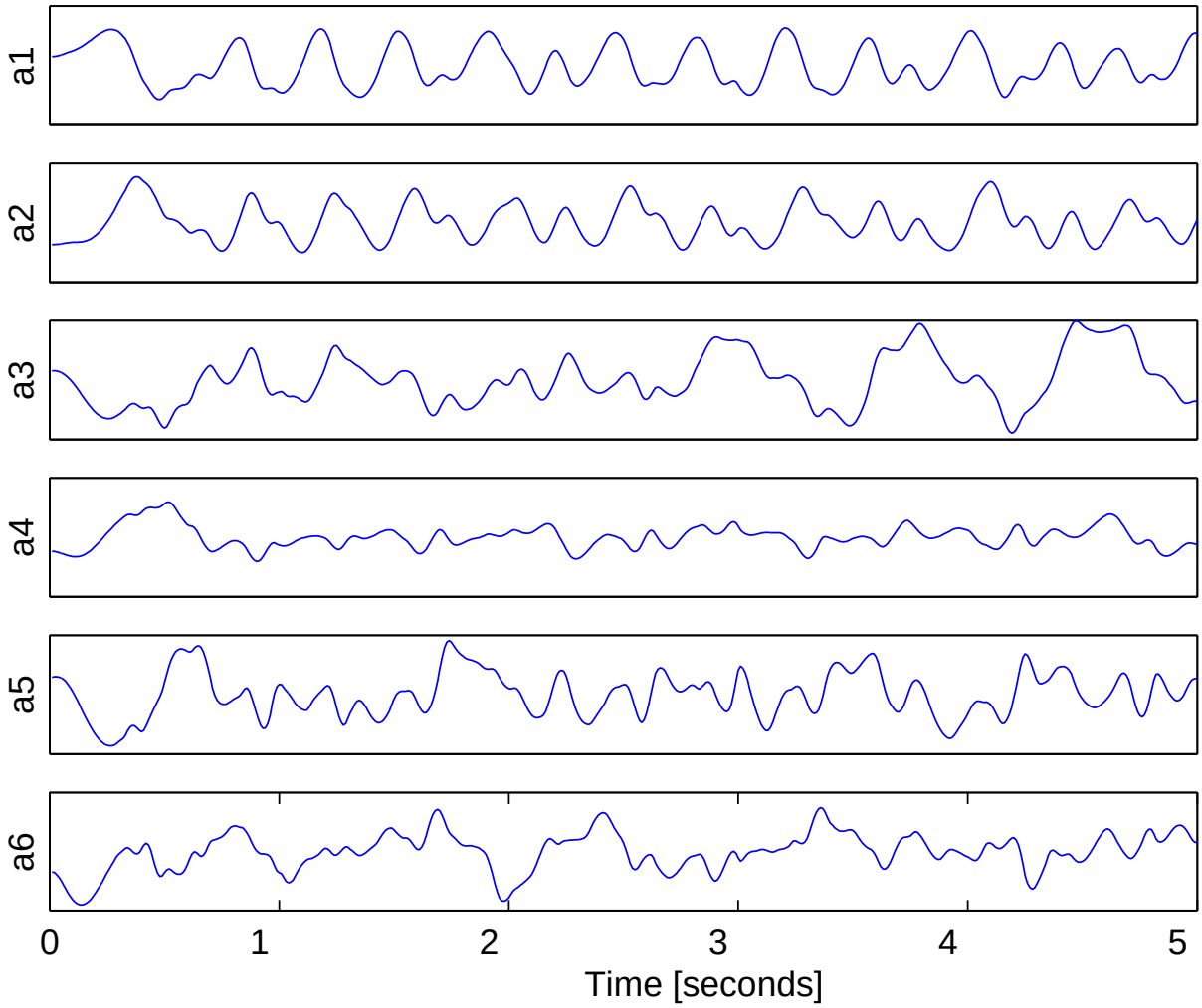


Figure 7: Case I. POD time series of ϵ_g.

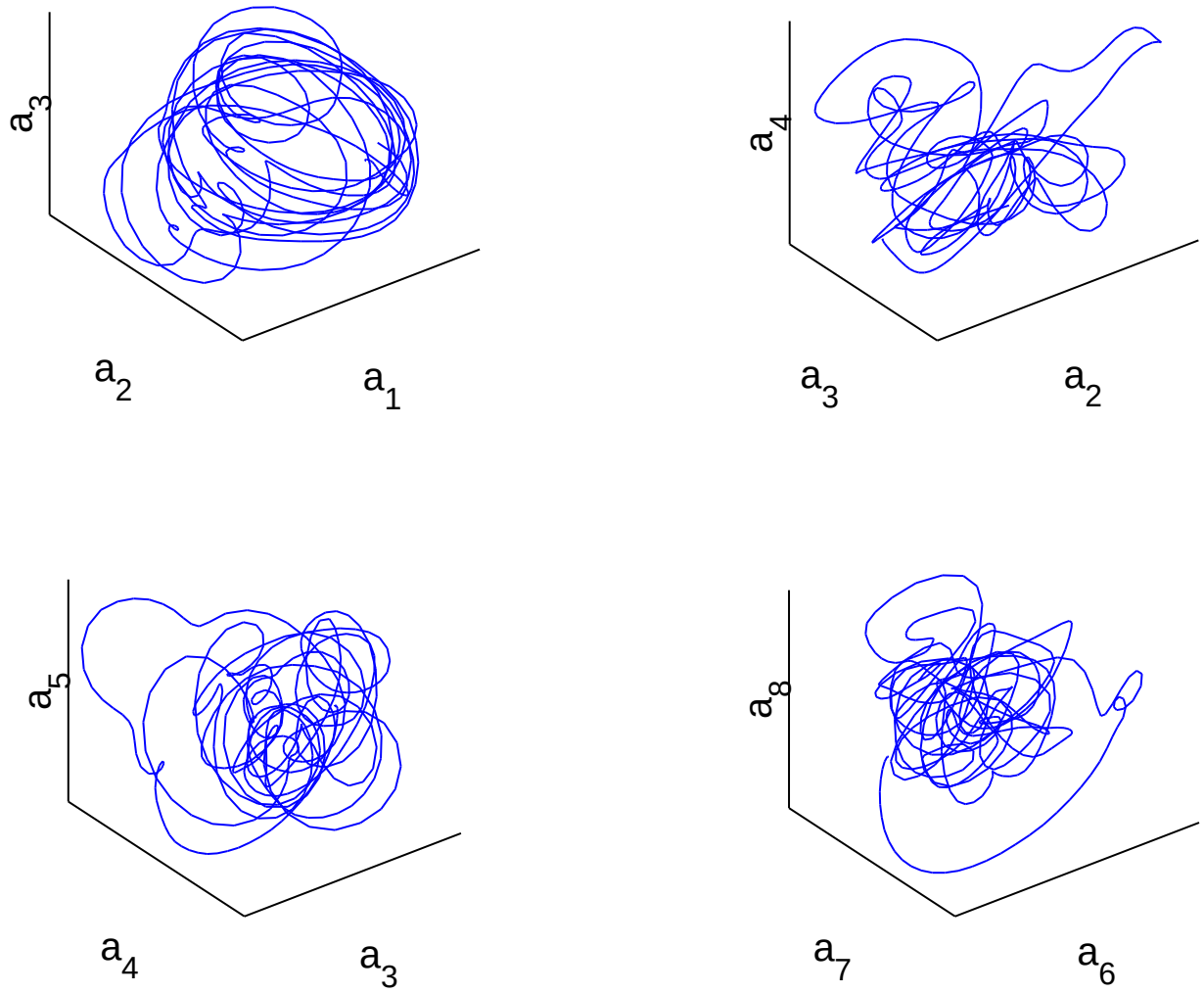


Figure 8: Case I. POD phase-space projections of ϵ_g.

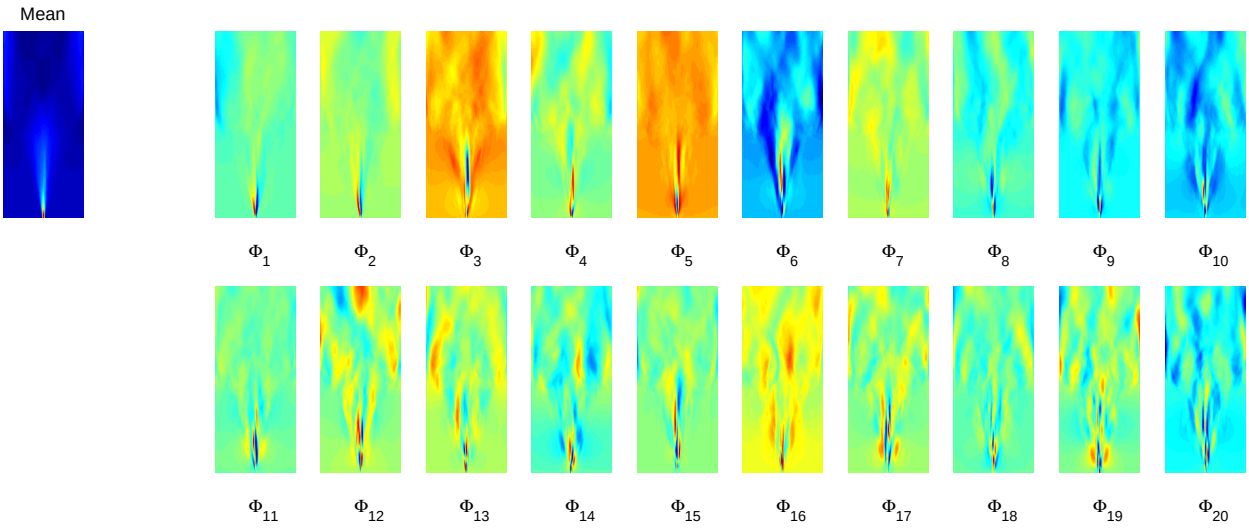


Figure 9: Case I. POD modes of V_g

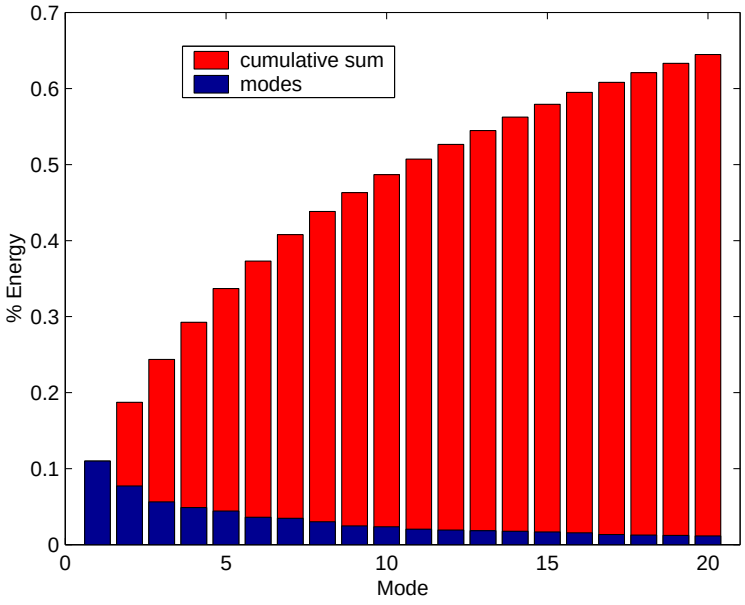


Figure 10: Case I. POD energy spectrum of V_g.

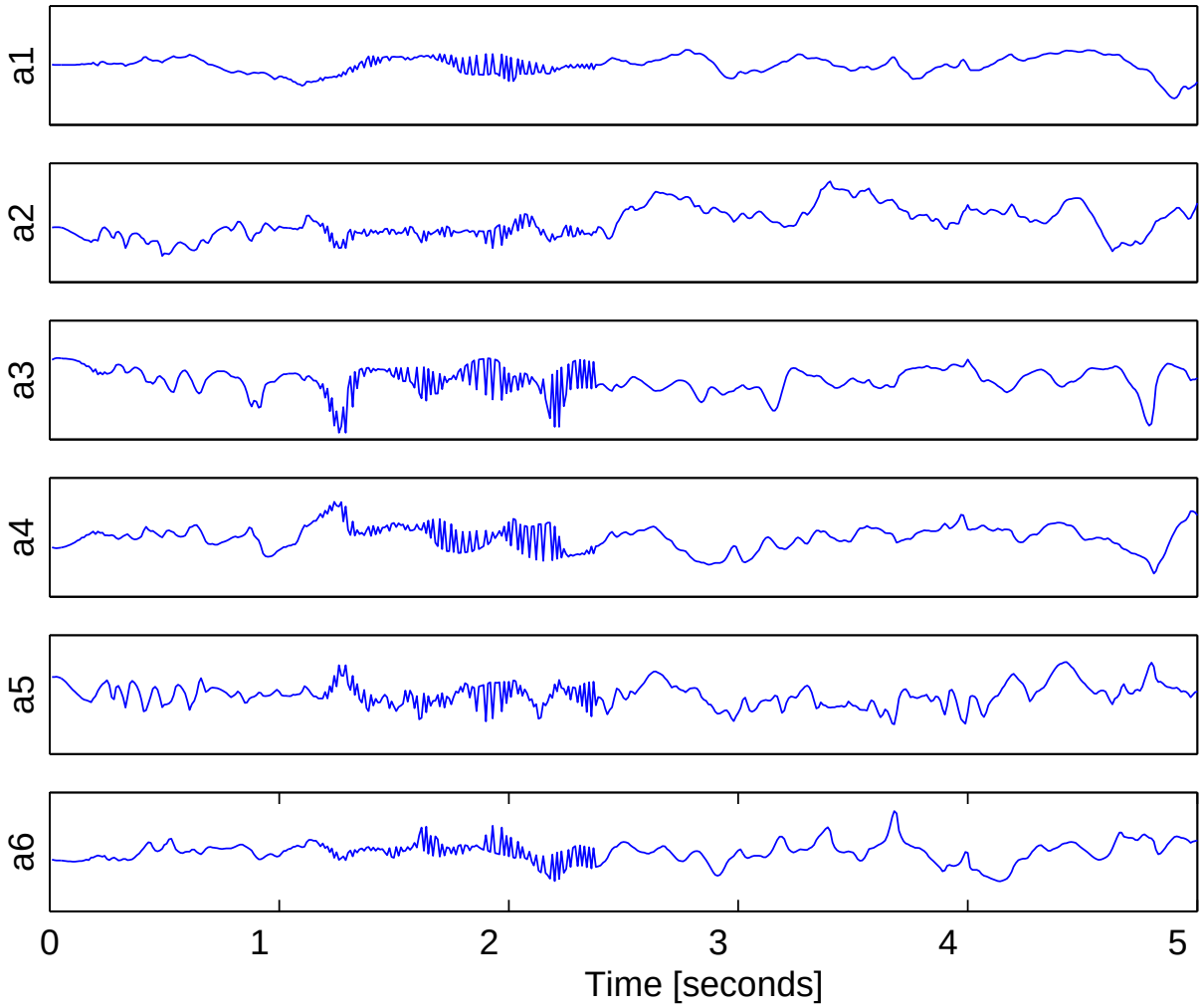


Figure 11: Case I. POD time series of V_g.

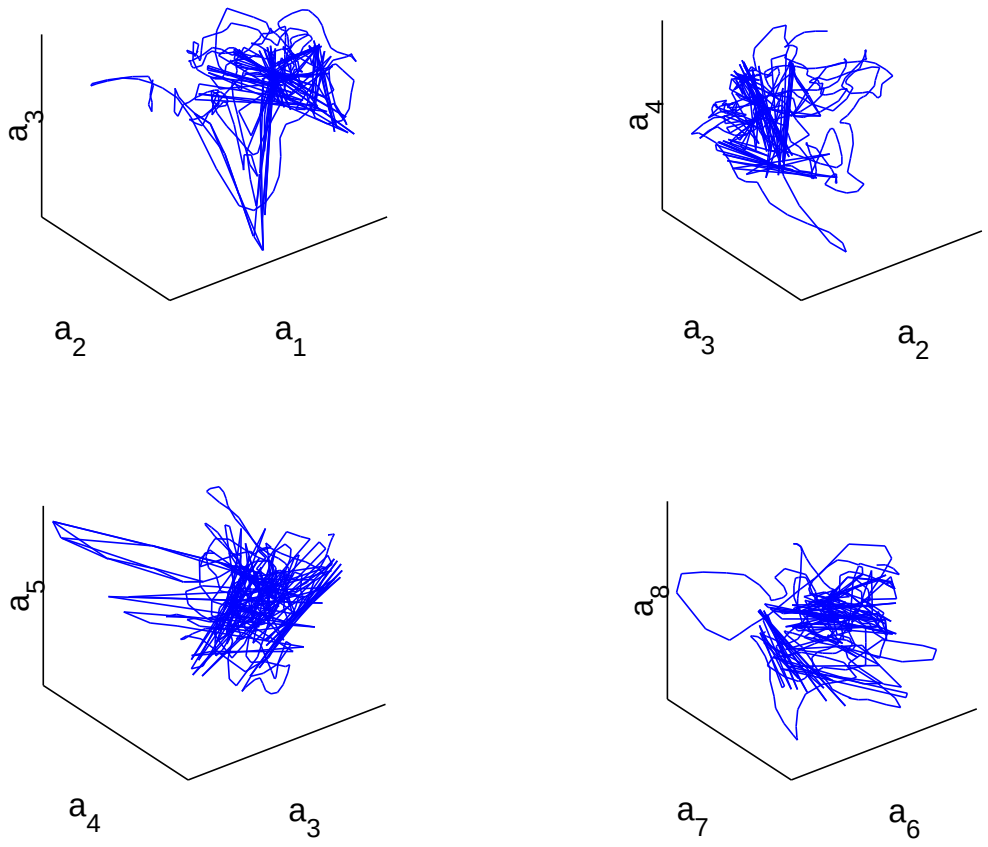


Figure 12: Case I. POD phase-space projections of V_g.

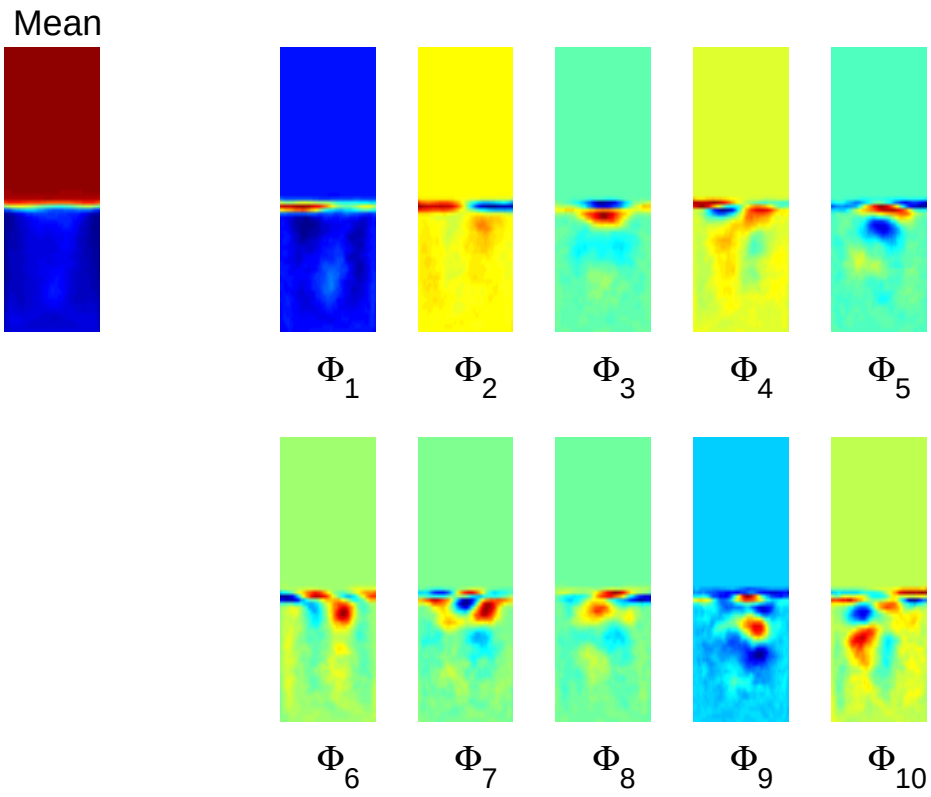


Figure 13: Case II. POD modes of ϵ_g

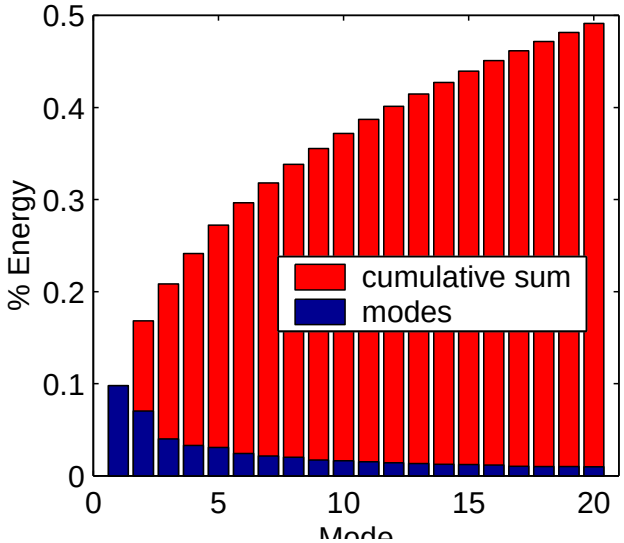


Figure 14: Case II. POD energy spectrum of ϵ_g.

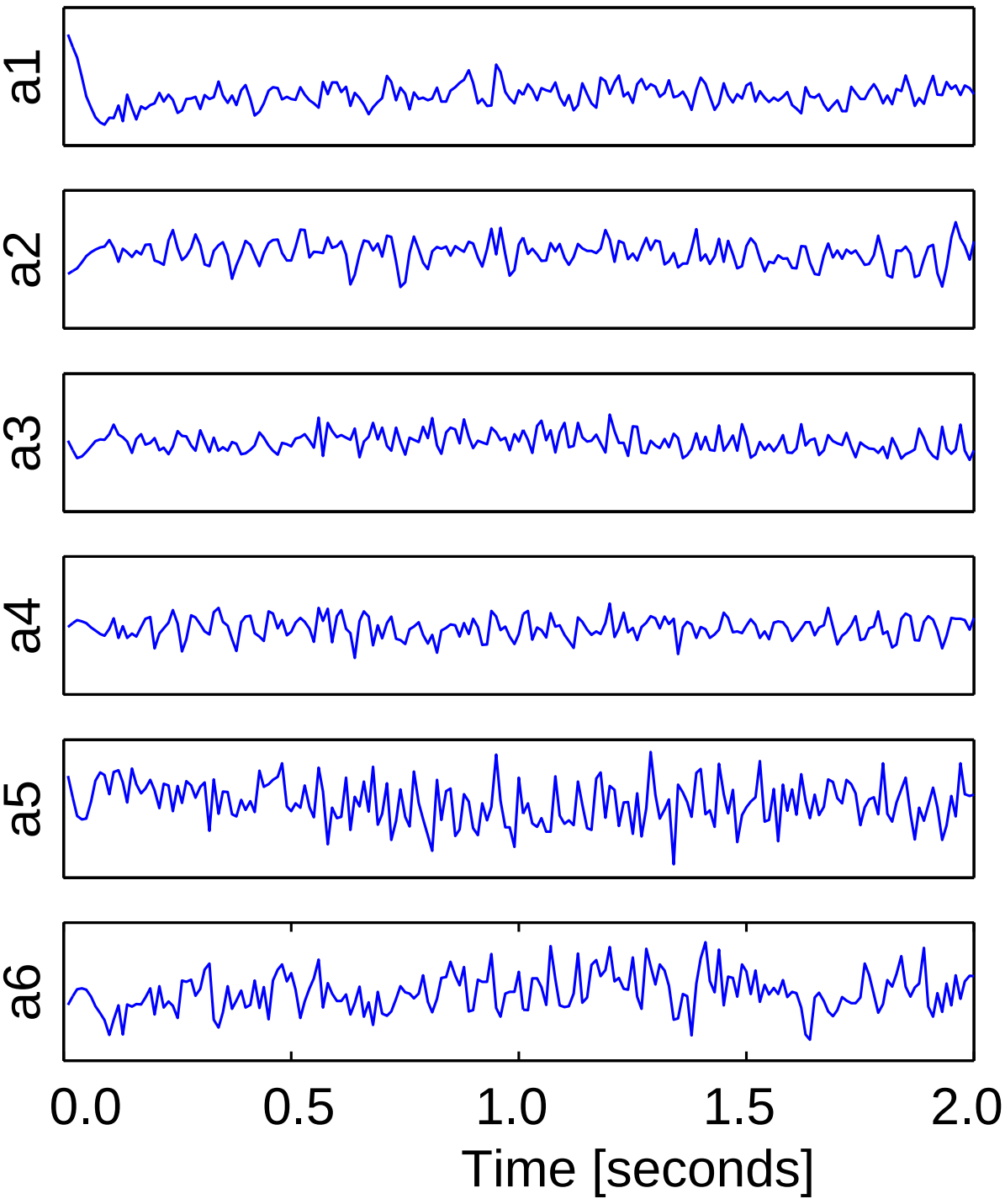


Figure 15: Case II. POD time series of ϵ_g.

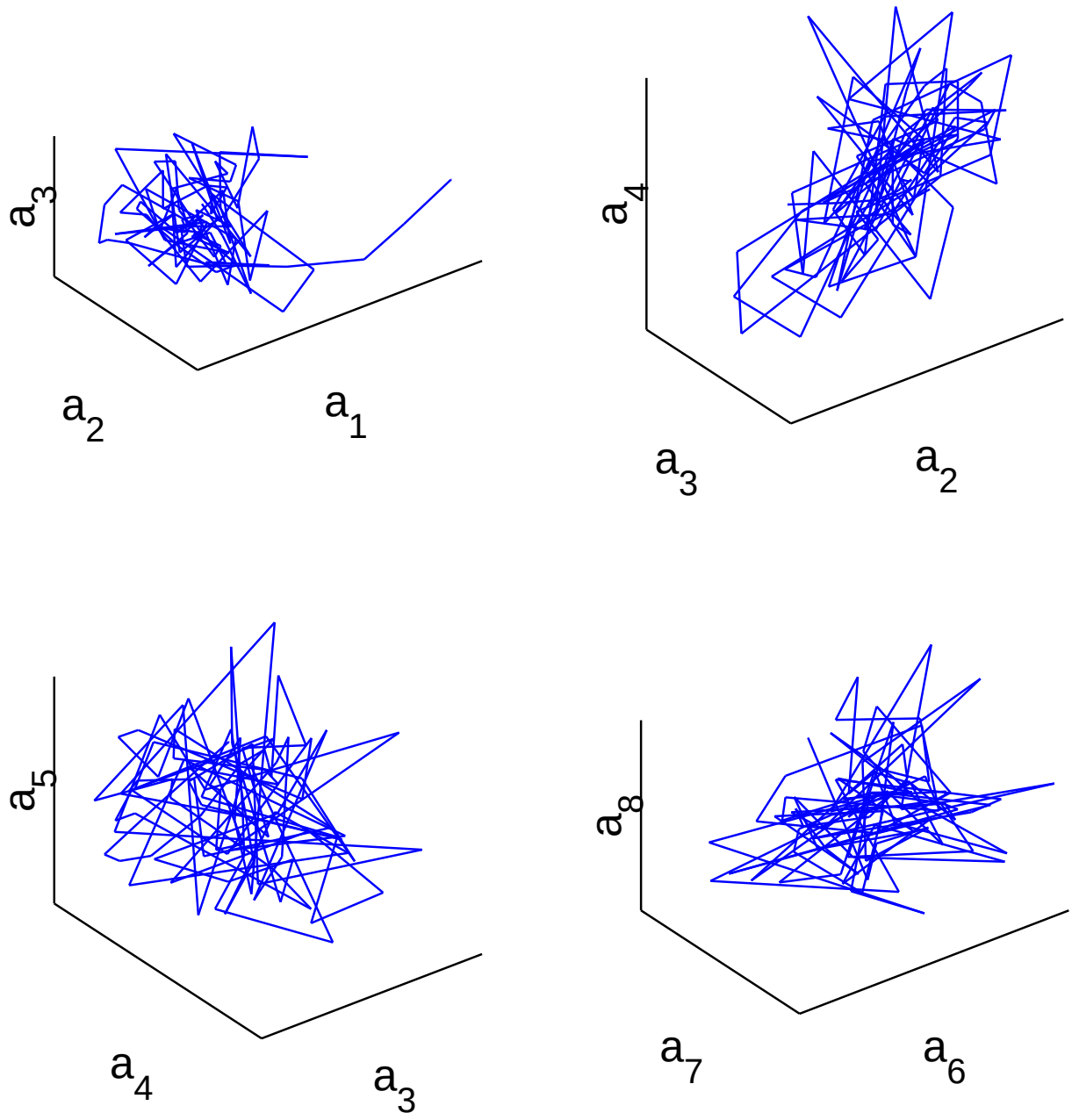


Figure 16: Case II. POD phase-space projections of ϵ_g.

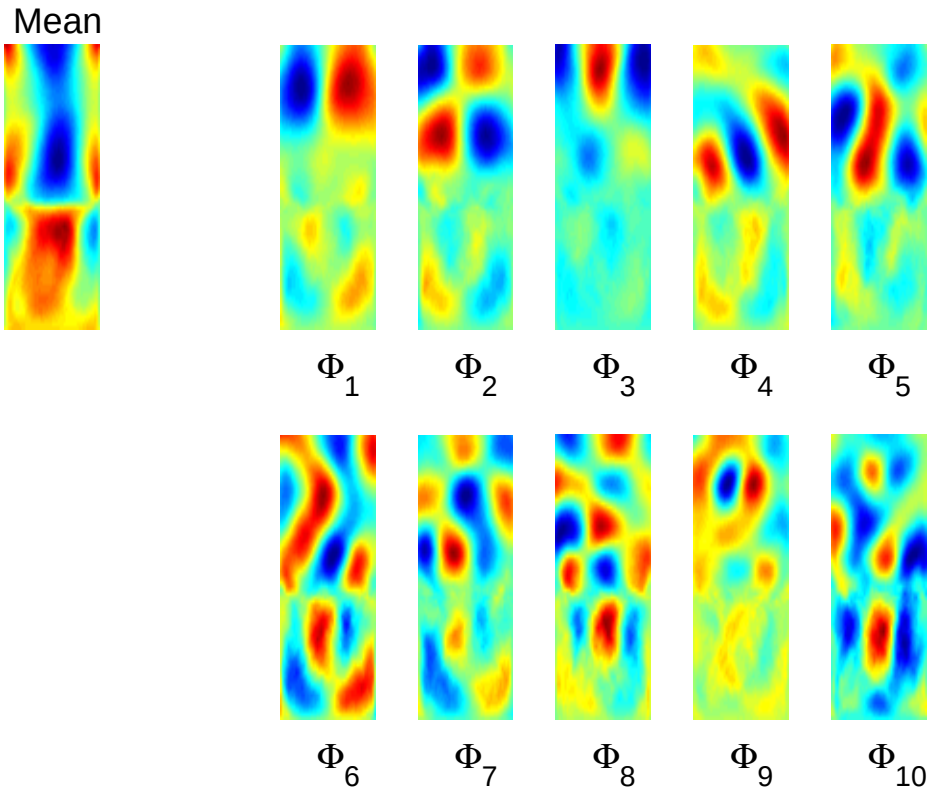


Figure 17: Case II. POD modes of V_g

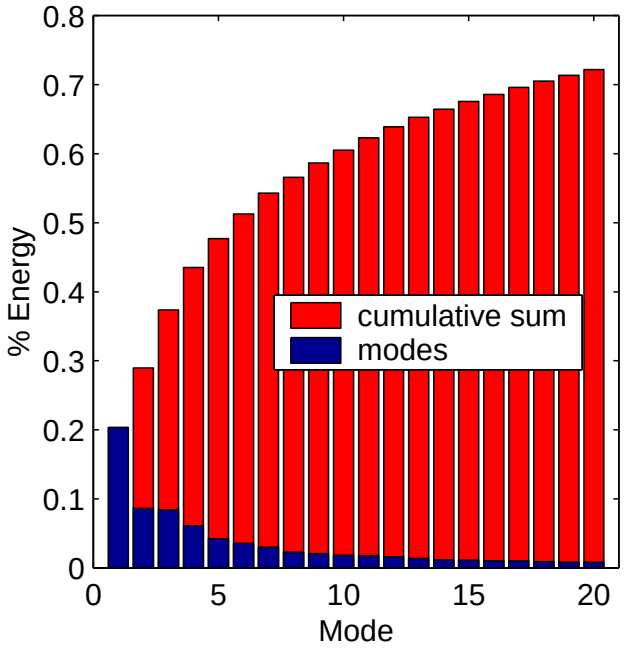


Figure 18: Case II. POD energy spectrum of V_g.

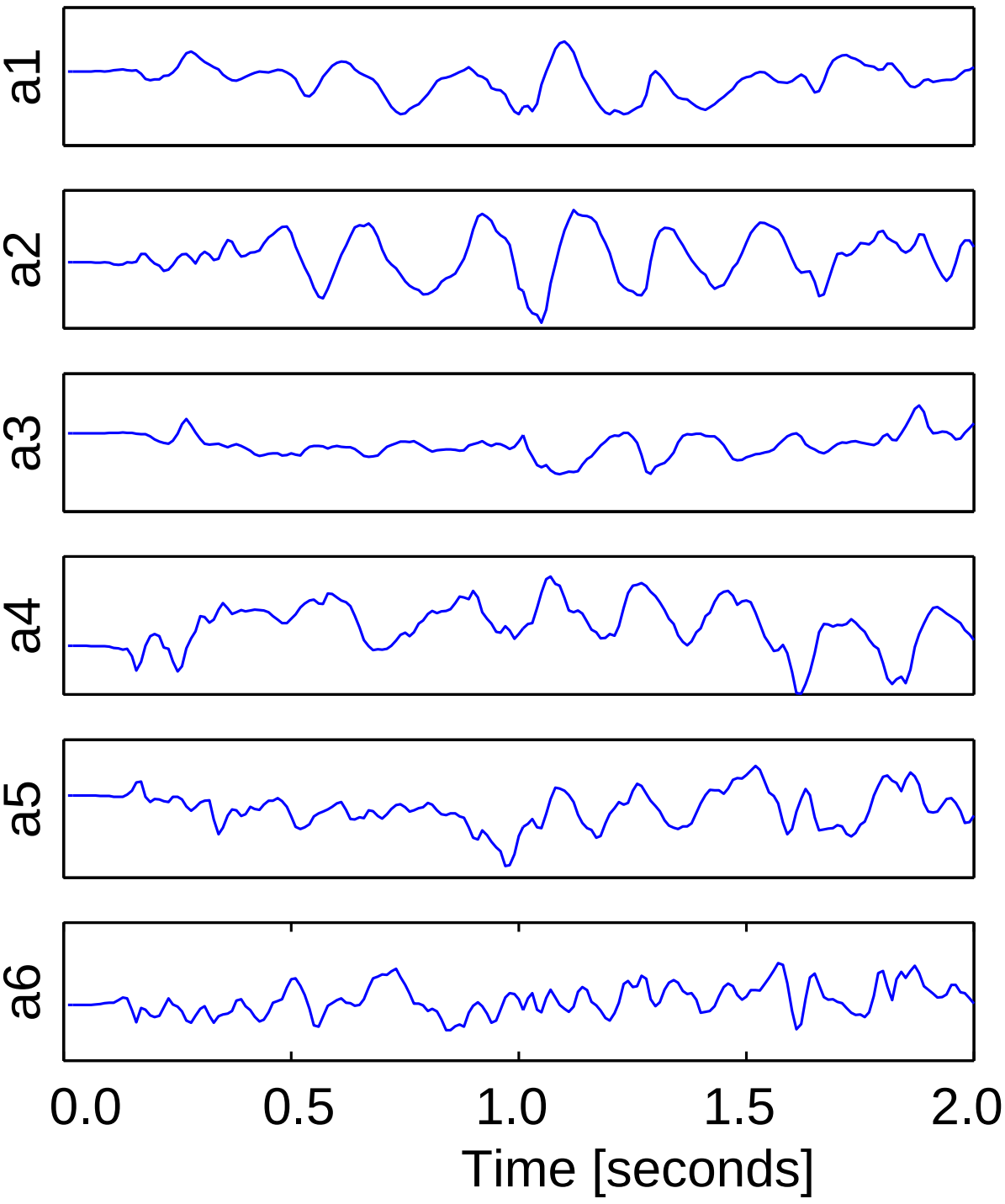


Figure 19: Case II. POD time series of V_g.

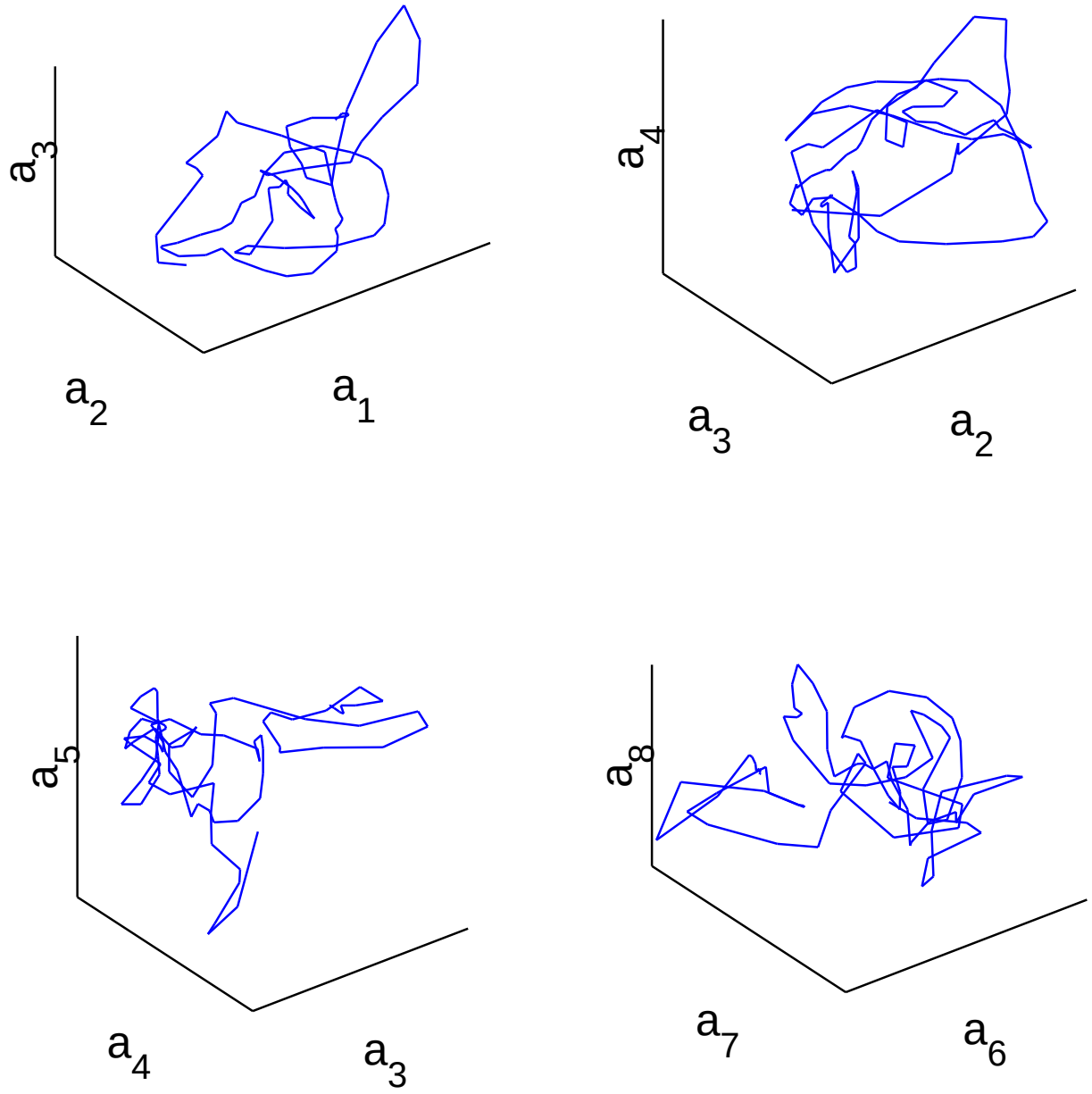


Figure 20: Case II. POD phase-space projections of V_g.

4.3 Visualization tools for the reconstruction of simulated data

The visualization tools include: (1) visualization of reconstructed flow motion, and (2) visualization of flow motion in phase space through POD time coefficients. Using POD spatial modes, visualizations of the reconstructed flow motion were generated. POD amplitude coefficients were used to create animations of the temporal behavior of the flow in phase space. A list of the computer codes developed for this task was presented in the second year report and is not included here.

4.4 Algorithm for reducing partial differential equations to ordinary differential equations

The development of an algorithm for reducing the partial differential equations (PDEs) to ordinary differential equations (ODEs) started by using the Navier-Stokes equations, a subset of the equations used in the MFIX code. Two approaches have been used for the derivation of the projected equations of mass, momentum and energy conservation: (1) using the governing equations written in primitive variables, and (2) using the governing equations written in conservative variables. It was concluded that using the primitive variables was the best option because this approach avoids quotients of sums. The sums were the result of replacing the flow variables by their POD decomposition.

Once it was decided to use primitive variables, several approaches have been used to project the PDEs onto the basis functions. In a first trial, the PDEs of the governing equations (mass and momentum for gas-only) were projected without taking into account the MFIX implementation, that is, using a discretization that did not take into account upwinding. The time coefficients obtained by solving the ODE system were compared against the time coefficients obtained directly from MFIX using the properties of the basis functions. The agreement was good only for a short period of time at startup.

The difference between the MFIX solution and the reconstructed solution was attributed to the fact that (1) the projected ODEs did not take into account upwinding, and (2) the ODEs were obtained using a differential form of the governing equations while MFIX used an integral form of the governing equations [3]. In addition, an investigation of the local accuracy of the MFIX results was done using the subroutine CHECK_CONVERGENCE provided by Dr. Madhava. It was found that the level of the local errors varied between 2 and 100%. These levels of the local error do not preclude the MFIX code from converging globally, but they could be a factor in altering the reconstructed solution.

The accuracy problem was further investigated. In order to generate the system of ODEs, the governing equations in MFIX must be rearranged. For example, the conservation of momentum in the x-direction, which in MFIX is written as

$$a_p u_p = \sum_{nb} a_{nb} u_{nb} + b - (P_E - P_W)\Delta y \tag{1}$$

must be rearranged in the reduced order model as

$$\rho_p^{old} \Delta V \frac{u_p - u_p^{old}}{\Delta t} = \sum_{nb} a_{nb}(u_{nb} - u_p) - (P_E - P_W)\Delta y. \tag{2}$$

Values of the left-hand-side (LHS) and right-hand-side (RHS) terms of equations (1) and (2) are shown in Table 1.

MFIX		Reduced Order Model	
LHS	RHS	LHS	RHS
-.839	-.827	-.136E-01	-.180E-02
-.778	-.767	-.127E-01	-.168E-02
-.715	-.705	-.117E-01	-.154E-02
-.650	-.641	-.106E-01	-.141E-02
-.583	-.575	-.956E-02	-.126E-02
-.514	-.507	-.843E-02	-.111E-02
-.766	-.755	-.124E-01	-.164E-02
-.711	-.701	-.115E-01	-.153E-02

Table 1: Values of left-hand-side and right-hand-side terms of the x-momentum conservation equation at different grid locations in MFIX and in the reduced order model.

The projection of the discretized equations consists basically of multiplying each LHS and RHS terms by the components of the POD basis vector and adding them. Although the difference between the LHS and RHS terms in the two columns is the same, the form used in the reduced order model for projections produces inaccurate results.

Two sets of reduced order models have been developed: (1) for gas-only flows, and (2) for gas-solids transport phenomena. The reduced order models for gas-only flows were developed first since they were easier to implement and verify. The knowledge acquired in the development of the reduced order models for gas-only flows was then used for the gas-solids model.

4.4.1 Reduced order model based on proper orthogonal decomposition for gas-only flows

For a two-dimensional gas-only flow problem, MFIX solves the gas x-momentum equation (3),

$$\begin{aligned}(a_m^u)_p(u_m)_p &= \sum_{nb}(a_m^u)_{nb}(u_m)_{nb} + (b_m^u)_p \\ &\quad -A_p(\epsilon_m)_p\left((p_g)_E - (p_g)_W\right) + \left(F_{gs}(u_l - u_m)_p\right)\Delta V, \end{aligned} \tag{3}$$

the gas y-momentum equation (4),

$$\begin{aligned}(a_m^v)_p(v_m)_p &= \sum_{nb}(a_m^v)_{nb}(v_m)_{nb} + (b_m^v)_p \\ &\quad -A_p(\epsilon_m)_p\left((p_g)_N - (p_g)_S\right) + \left(F_{gs}(v_l - v_m)_p\right)\Delta V, \end{aligned} \tag{4}$$

and the gas pressure correction equation (5)

$$a_P^p(p_g')_P = \sum_{nb} a_{nb}^p(p_g')_{nb} + b_P^p. \tag{5}$$

For gas-only flow problems, $\epsilon_g \equiv 1$, $\epsilon_s \equiv 0$, and $F_{gs} \equiv 0$. The dependent field variables are the gas pressure p_g and the gas velocities u_g and v_g. The subscript g is dropped for convenience when describing the POD-based ROMs for gas-only flows. Table 2 lists the features of the POD-based

ROMs generated for gas-only flows. The ODExMIN model is not included since it is similar to ODExNL, except for the solution methodology. The following sections will present in detail the newest and best performing models: ODExMFIX and ODEx3. The other models were described in the second year report.

Table 2: Reduced order models for gas-only flows

Model	Governing Equations	ROM Equations	ROM Unknowns	Assumptions
ODEx	x-momentum balance y-momentum balance	ODEs	α^u, α^v	ρ, p, T=const.
ODExNL	x-momentum balance y-momentum balance	nonlinear	α^u, α^v	ρ, p, T=const.
ODExMFIX	x-momentum balance y-momentum balance pressure correction	linear	α^u, α^v, α^p	T=const.
ODEx3	x-momentum balance y-momentum balance mass balance	ODEs	α^u, α^v, α^ρ	T=const.

4.4.1.1 ODExMFIX ODExMFIX is a POD-based ROM generated to model gas-only flows. ODExMFIX is derived from the discretized momentum equations (3), (4) and the gas pressure correction equation (5). The discretized momentum equations and the gas pressure correction equation are rearranged as

$$a_p^u u_p - \sum_{nb} a_{nb}^u u_{nb} = b_p^u - \Delta y(p_E - p_W), \tag{6}$$

$$a_p^v v_p - \sum_{nb} a_{nb}^v v_{nb} = b_p^v - \Delta x(p_N - p_S), \tag{7}$$

$$a_p^p p_p' - \sum_{nb} a_{nb}^p p_{nb}' = b_p^p. \tag{8}$$

where the subscript nb represents E, W, N, and S, as shown in Fig. 21. In ODExMFIX, p, u, and v are approximated using the POD basis functions as

$$u(\mathbf{x}, t) = \bar{u}(\mathbf{x}) + u'(\mathbf{x}, t) \cong \phi_0^u(\mathbf{x}) + \sum_{i=1}^{m^u} \alpha_i^u(t)\phi_i^u(\mathbf{x}), \tag{9}$$

$$v(\mathbf{x}, t) = \bar{v}(\mathbf{x}) + v'(\mathbf{x}, t) \cong \phi_0^v(\mathbf{x}) + \sum_{i=1}^{m^v} \alpha_i^v(t)\phi_i^v(\mathbf{x}), \tag{10}$$

$$p(\mathbf{x}, t) \cong \phi_0^p(\mathbf{x}) + \sum_{i=1}^{m^p} \alpha_i^p(t)\phi_i^p(\mathbf{x}). \tag{11}$$

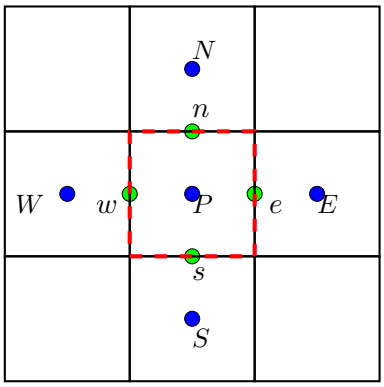


Figure 21: Control volume for mass balance

where m^u, m^v, and m^p are the number of POD modes used to approximate u, v, and p, respectively. The correction of the pressure, p', is approximated as

$$p'(\mathbf{x},t) \cong \sum_{i=1}^{m^p} (\alpha_i^p)'(t)\phi_i^p(\mathbf{x}). \tag{12}$$

Substituting the approximations of u, v, and p' given by (9), (10), and (12) into equations (6), (7), and (8), respectively, yields

$$a_p^u \sum_{i=0}^{m^u} \alpha_i^u \phi_i^u - \sum_{nb} a_{nb}^u \sum_{i=0}^{m^u} \alpha_i^u \phi_{i,nb}^u = b_p^u - \Delta y(p_E - p_W), \tag{13}$$

$$a_p^v \sum_{i=0}^{m^v} \alpha_i^v \phi_i^v - \sum_{nb} a_{nb}^v \sum_{i=0}^{m^v} \alpha_i^v \phi_{i,nb}^v = b_p^v - \Delta x(p_N - p_S), \tag{14}$$

$$a_p^p \sum_{i=1}^{m^p} (\alpha_i^p)' \phi_i^p - \sum_{nb} a_{nb}^p \sum_{i=1}^{m^p} (\alpha_i^p)' \phi_{i,nb}^p = b_p^p. \tag{15}$$

Projecting equations (13), (14), and (15) onto the basis functions ϕ_k^u, ϕ_k^v, and ϕ_k^p, respectively, generates three systems of linear equations:

$$\tilde{\mathcal{A}}^u \alpha^u = \tilde{\mathcal{B}}^u, \tag{16}$$

$$\tilde{\mathcal{A}}^v \alpha^v = \tilde{\mathcal{B}}^v, \tag{17}$$

$$\tilde{\mathcal{A}}^p \alpha^p = \tilde{\mathcal{B}}^p, \tag{18}$$

where

$$\tilde{\mathcal{A}}_{ij}^u = \left((a_p^u \phi_j^u - \sum_{nb} a_{nb}^u \phi_{j,nb}^u),\ \phi_i^u \right),$$

$$\tilde{\mathcal{B}}_i^u = \left([b_p^u - \Delta y(p_E - p_W) - (a_p^u \phi_0^u - \sum_{nb} a_{nb}^u \phi_{0,nb}^u)],\ \phi_i^u \right),$$

$$\tilde{\mathcal{A}}_{ij}^v = \left((a_p^v \phi_j^v - \sum_{nb} a_{nb}^v \phi_{j,nb}^v),\ \phi_i^v \right),$$

$$\tilde{\mathcal{B}}_i^v = \left([b_p^v - \Delta x(p_N - p_S) - (a_p^v \phi_0^v - \sum_{nb} a_{nb}^v \phi_{0,nb}^v)],\ \phi_i^v \right),$$

$$\tilde{\mathcal{A}}_{ij}^p = \left((a_p^p \phi_j^p - \sum_{nb} a_{nb}^p \phi_{j,nb}^p),\ \phi_i^p \right),$$

$$\tilde{\mathcal{B}}_i^p = \left(b_p^p,\ \phi_i^p \right).$$

The dimensions of $\tilde{\mathcal{A}}^u$, $\tilde{\mathcal{A}}^v$ and $\tilde{\mathcal{A}}^p$ are $m^u \times m^u$, $m^v \times m^v$, and $m^p \times m^p$, respectively. The dimensions of $\tilde{\mathcal{B}}^u$, $\tilde{\mathcal{B}}^v$ and $\tilde{\mathcal{B}}^p$ are $m^u \times 1$, $m^v \times 1$, and $m^p \times 1$, respectively. These matrices are calculated using the field variables from the previous iteration. The systems of linear equations (16), (17), and (18) are solved using the LU decomposition method.

ODExMFIX uses an iterative algorithm which is similar to the algorithm used in MFIX. An outline of the solution algorithm in ODExMFIX is given below:

- Using the time coefficients from the previous iteration, reconstruct the field variables p, u and v. For compressible flows, calculate the density ρ using the ideal gas law.
- Solve the system of linear equations (16) and obtain the tentative values of $\alpha_i^u(t)$, $i \in [1, m^u]$. The values are called tentative values because they are calculated based on the previous pressure field and they will be corrected based on the pressure correction.
- Solve the system of linear equations (17) and obtain the tentative values of $\alpha_i^v(t)$, $i \in [1, m^v]$.
- Solve the system of linear equations (18) and obtain $(\alpha_i^p)'(t)$, $i \in [1, m^p]$.
- Correct the time coefficients of p, u and v.
- Check the convergence. If converged, advance to the next time step.

The input data for ODExMFIX are the basis functions of the velocities and the pressure. The solutions of ODExMFIX are α_i^u, $i \in [1, m^u]$, α_i^v, $i \in [1, m^v]$, and α_i^p, $i \in [1, m^p]$. An example of the input file of ODExMFIX is presented in Appendix A.

4.4.1.2 ODEx3 ODEx3 is a POD-based ROM generated to model compressible gas flows. ODEx3 is derived from the discretized gas mass equation (19)

$$(a_m)_P (\epsilon_m \rho_m)_P = \sum_{nb} (a_m)_{nb} (\epsilon_m \rho_m)_{nb} + (b_m)_P, \tag{19}$$

and the discretized gas momentum equations (3) and (4). For gas-only flows the dependent variables in MFIX are the pressure p and the velocities u and v. The density field is calculated from the pressure field using the ideal gas law (20)

$$\rho = \frac{p\mathcal{M}}{\mathcal{R}T}, \tag{20}$$

where $\mathcal{M}$ is the molecular mass and $\mathcal{R}$ is the universal gas constant. ρ is approximated using the basis functions ϕ_i^ρ, $i \in [1, m^\rho]$ as

$$\rho \cong \phi_0^\rho + \sum_{i=1}^{m^\rho} \alpha_i^\rho(t)\phi_i^\rho. \tag{21}$$

Consequently, the pressure p is approximated as

$$p \cong \frac{\mathcal{R}T}{\mathcal{M}} \left(\phi_0^\rho + \sum_{i=1}^{m^\rho} \alpha_i^\rho(t)\phi_i^\rho \right). \tag{22}$$

Herein $(a_m)_P$, $(a_m)_{nb}$, and $(b_m)_P$ are defined as

$$\begin{aligned}
(a_m)_E &= -(\xi_m)_e(u_m)_e A_e, \\
(a_m)_W &= (\bar{\xi}_m)_w(u_m)_w A_w, \\
(a_m)_N &= -(\xi_m)_n(v_m)_n A_n, \\
(a_m)_S &= (\bar{\xi}_m)_s(v_m)_s A_s, \\
(a_m)_P &= \frac{\Delta V}{\Delta t} + ((u_m)_e A_e - (u_m)_w A_w + (v_m)_n A_n - (v_m)_s A_s) + \sum_{nb}(a_m)_{nb}, \\
(b_m)_P &= (\epsilon_m \rho_m)_P^o \frac{\Delta V}{\Delta t},
\end{aligned} \tag{23}$$

where A, ΔV, and Δt denote the face area, cell volume, and time step size, respectively. The superscript o denotes old (previous) time step values.

Using equations (23), the discretized gas mass equation (19) is rearranged as

$$\begin{aligned}
\Delta V \cdot \frac{\rho_P - \rho_P^o}{\Delta t} &= -(\xi_e\rho_E + \bar{\xi}_e\rho_P)u_e\Delta y + (\xi_w\rho_P + \bar{\xi}_w\rho_W)u_w\Delta y \\
&\quad -(\xi_n\rho_N + \bar{\xi}_n\rho_P)v_n\Delta x + (\xi_s\rho_P + \bar{\xi}_s\rho_S)v_s\Delta x,
\end{aligned} \tag{24}$$

where $\Delta y = A_e = A_w$ and $\Delta x = A_n = A_s$ for two-dimensional flows. Replacing $\frac{\rho_P - \rho_P^o}{\Delta t}$ by $\frac{\partial \rho}{\partial t}$ and

substituting the approximations given by (9), (10), and (21) into equation (24), one obtains

$$\begin{aligned}\Delta V \sum_{i=1}^{m^\rho} \dot{\alpha}_i^\rho \phi_i^\rho &= -\sum_{i=0}^{m^\rho}\sum_{j=0}^{m^u}(\xi_e\phi_{i,E}^\rho + \bar{\xi}_e\phi_i^\rho)\phi_j^u \cdot \alpha_i^\rho\alpha_j^u + \\ &+ \sum_{i=0}^{m^\rho}\sum_{j=0}^{m^u}(\xi_w\phi_i^\rho + \bar{\xi}_w\phi_{i,W}^\rho)\phi_{j,w}^u \cdot \alpha_i^\rho\alpha_j^u - \\ &- \sum_{i=0}^{m^\rho}\sum_{j=0}^{m^v}(\xi_n\phi_{i,N}^\rho + \bar{\xi}_n\phi_i^\rho)\phi_j^v \cdot \alpha_i^\rho\alpha_j^v + \\ &+ \sum_{i=0}^{m^\rho}\sum_{j=0}^{m^v}(\xi_s\phi_i^\rho + \bar{\xi}_s\phi_{i,S}^\rho)\phi_{j,s}^v \cdot \alpha_i^\rho\alpha_j^v. \end{aligned} \tag{25}$$

Projecting equation (25) onto the basis functions ϕ_k^ρ, $k \in [1, m^\rho]$, generates m^ρ ODEs

$$\check{\mathcal{A}}_{kk}^\rho \dot{\alpha}_k^\rho = \sum_{i=0}^{m^\rho}\sum_{j=0}^{m^u}\check{\mathcal{F}}_{kij}^\rho \alpha_i^\rho\alpha_j^u + \sum_{i=0}^{m^\rho}\sum_{j=0}^{m^v}\check{\mathcal{G}}_{kij}^\rho \alpha_i^\rho\alpha_j^v, \tag{26}$$

where

$$\check{\mathcal{A}}_{ij}^\rho = \delta_{ij} \cdot \Delta V,$$

$$\check{\mathcal{F}}_{kij}^\rho = -\left((\xi_e\phi_{i,E}^\rho + \bar{\xi}_e\phi_i^\rho)\phi_j^u,\ \phi_k^\rho\right) + \left((\xi_w\phi_i^\rho + \bar{\xi}_w\phi_{i,W}^\rho)\phi_{j,w}^u,\ \phi_k^\rho\right),$$

$$\check{\mathcal{G}}_{kij}^\rho = -\left((\xi_n\phi_{i,N}^\rho + \bar{\xi}_n\phi_i^\rho)\phi_j^v,\ \phi_k^\rho\right) + \left((\xi_s\phi_i^\rho + \bar{\xi}_s\phi_{i,S}^\rho)\phi_{j,s}^v,\ \phi_k^\rho\right).$$

For compressible gas flows, the discretized momentum equations are

$$a_p^u u_p = \sum_{nb} a_{nb}^u u_{nb} + b_p^u - \Delta y(p_E - p_W), \tag{27}$$

$$a_p^v v_p = \sum_{nb} a_{nb}^v v_{nb} + b_p^v - \Delta x(p_N - p_S). \tag{28}$$

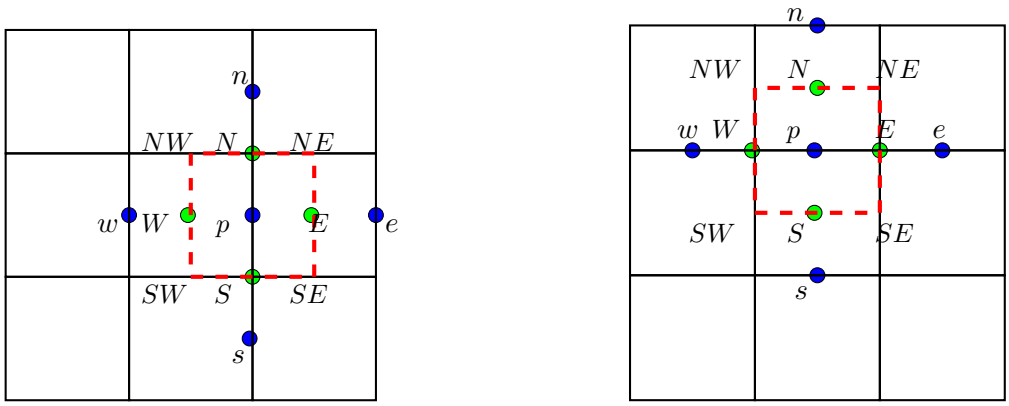
Figures 22(a) and 22(b) show the control volumes used in MFIX to discretize the x-momentum balance equation and y-momentum balance equation, respectively. In Figures 22(a) and 22(b), p denotes the center of the control volume; e, w, n, and s represent the east, west, north, and south neighbor cells of the control volume; E, W, N, and S denote the east, west, north, and south faces of the control volume; NE, NW, SE, and SW denote the four corners of the control volume.

Substituting equations

$$(a_\ell^u)_p = \sum_{nb}(a_\ell^u)_{nb} + (a_\ell^u)_p^o, \tag{29}$$

$$(a_\ell^u)_p^o = \frac{(\epsilon_\ell\rho_\ell)_p^o \Delta V}{\Delta t} \tag{30}$$

$$(b_\ell^u)_p = (a_\ell^u)_p^o (u_\ell)_p^o + S_\ell^u, \tag{31}$$



(a) x-momentum balance

(b) y-momentum balance

Figure 22: Control volume for momentum balance

where ℓ denotes the phase (here is gas), into equation (27) and substituting equations

$$(a_\ell^v)_p = \sum_{nb}(a_\ell^v)_{nb} + (a_\ell^v)_p^o, \tag{32}$$

$$(a_\ell^v)_p^o = \frac{(\epsilon_\ell \rho_\ell)_p^o \Delta V}{\Delta t}, \tag{33}$$

$$(b_\ell^v)_p = (a_\ell^v)_p^o (v_\ell)_p^o + S_\ell^v - (\epsilon_\ell \rho_m)_p g \Delta V, \tag{34}$$

into equation (28) yields

$$\left(\sum_{nb} a_{nb}^u + \frac{\rho_p^o \Delta V}{\Delta t}\right) u_p = \sum_{nb} a_{nb}^u u_{nb} + \frac{\rho_p^o \Delta V}{\Delta t} u_p^o + S^u - \Delta y(p_E - p_W), \tag{35}$$

$$\left(\sum_{nb} a_{nb}^v + \frac{\rho_p^o \Delta V}{\Delta t}\right) v_p = \sum_{nb} a_{nb}^v v_{nb} + \frac{\rho_p^o \Delta V}{\Delta t} v_p^o - \rho_p g \Delta V + S^v - \Delta x(p_N - p_S). \tag{36}$$

Equations (35) and (36) are rearranged as

$$\rho_p^o \Delta V \frac{u_p - u_p^o}{\Delta t} = \sum_{nb} a_{nb}^u (u_{nb} - u_p) + S^u - \Delta y(p_E - p_W), \tag{37}$$

$$\rho_p^o \Delta V \frac{v_p - v_p^o}{\Delta t} = \sum_{nb} a_{nb}^v (v_{nb} - v_p) - \rho_p g \Delta V + S^v - \Delta x(p_N - p_S). \tag{38}$$

Replacing $\frac{u_p - u_p^o}{\Delta t}$ and $\frac{v_p - v_p^o}{\Delta t}$ by $\frac{\partial u_p}{\partial t}$ and $\frac{\partial v_p}{\partial t}$, respectively, yields

$$\rho_p^o \Delta V \frac{\partial u_p}{\partial t} = \sum_{nb} a_{nb}^u (u_{nb} - u_p) + S^u - \Delta y(p_E - p_W), \tag{39}$$

$$\rho_p^o \Delta V \frac{\partial v_p}{\partial t} = \sum_{nb} a_{nb}^v (v_{nb} - v_p) - \rho_p g \Delta V + S^v - \Delta x (p_N - p_S). \tag{40}$$

Substituting the approximations of u, v, ρ and p given by equations (9), (10), (21), and (22) and the definitions of a_{nb}^u and a_{nb}^v given by equations

$$(a_\ell^u)_e = \frac{(\mu_\ell)_E A_E}{\Delta x} - (\xi_\ell^u)_e (\epsilon_\ell \rho_\ell)_e (u_\ell)_E A_E, \tag{41}$$

$$(a_\ell^u)_w = \frac{(\mu_\ell)_W A_W}{\Delta x} + (\bar{\xi}_\ell^u)_w (\epsilon_\ell \rho_\ell)_w (u_\ell)_W A_W, \tag{42}$$

$$(a_\ell^u)_n = \frac{(\mu_\ell)_N A_N}{\Delta y} - (\xi_\ell^u)_n (\epsilon_\ell \rho_\ell)_n (v_\ell)_N A_N, \tag{43}$$

$$(a_\ell^u)_s = \frac{(\mu_\ell)_S A_S}{\Delta y} + (\bar{\xi}_\ell^u)_s (\epsilon_\ell \rho_\ell)_s (v_\ell)_S A_S, \tag{44}$$

$$(a_\ell^u)_p = \sum_{nb} (a_\ell^u)_{nb} + (a_\ell^u)_p^o, \tag{45}$$

$$(a_\ell^u)_p^o = \frac{(\epsilon_\ell \rho_\ell)_p^o \Delta V}{\Delta t}, \tag{46}$$

and equations

$$(a_\ell^v)_e = \frac{(\mu_\ell)_E A_E}{\Delta x} - (\xi_\ell^v)_e (\epsilon_\ell \rho_\ell)_e (u_\ell)_E A_E, \tag{47}$$

$$(a_\ell^v)_w = \frac{(\mu_\ell)_W A_W}{\Delta x} + (\bar{\xi}_\ell^v)_w (\epsilon_\ell \rho_\ell)_w (u_\ell)_W A_W, \tag{48}$$

$$(a_\ell^v)_n = \frac{(\mu_\ell)_N A_N}{\Delta y} - (\xi_\ell^v)_n (\epsilon_\ell \rho_\ell)_n (v_\ell)_N A_N, \tag{49}$$

$$(a_\ell^v)_s = \frac{(\mu_\ell)_S A_S}{\Delta y} + (\bar{\xi}_\ell^v)_s (\epsilon_\ell \rho_\ell)_s (v_\ell)_S A_S, \tag{50}$$

into equations (39) and (40), yields

$$\begin{aligned}
\rho_p^o \Delta V \cdot \sum_{i=1}^{m^u} \dot{\alpha}_i^u \phi_i^u &= -\sum_{i=0}^{m^\rho}\sum_{j=0}^{m^u}\sum_{k=0}^{m^u} \xi_E^u \phi_{i,e}^\rho \phi_{k,E}^u (\phi_{j,e}^u - \phi_j^u)\Delta y \alpha_i^\rho \alpha_j^u \alpha_k^u \\
&+ \sum_{i=0}^{m^\rho}\sum_{j=0}^{m^u}\sum_{k=0}^{m^u} \bar{\xi}_W^u \phi_{i,w}^\rho \phi_{k,W}^u (\phi_{j,w}^u - \phi_j^u)\Delta y \alpha_i^\rho \alpha_j^u \alpha_k^u \\
&- \sum_{i=0}^{m^\rho}\sum_{j=0}^{m^u}\sum_{k=0}^{m^v} \xi_N^u \phi_{i,n}^\rho \phi_{k,N}^v (\phi_{j,n}^u - \phi_j^u)\Delta x \alpha_i^\rho \alpha_j^u \alpha_k^v \\
&+ \sum_{i=0}^{m^\rho}\sum_{j=0}^{m^u}\sum_{k=0}^{m^v} \bar{\xi}_S^u \phi_{i,s}^\rho \phi_{k,S}^v (\phi_{j,s}^u - \phi_j^u)\Delta x \alpha_i^\rho \alpha_j^u \alpha_k^v \\
&+ \sum_{i=0}^{m^u} \frac{\mu_E \Delta y}{\Delta x}(\phi_{i,e}^u - \phi_i^u)\alpha_i^u + \sum_{i=0}^{m^u} \frac{\mu_W \Delta y}{\Delta x}(\phi_{i,w}^u - \phi_i^u)\alpha_i^u \\
&+ \sum_{i=0}^{m^u} \frac{\mu_N \Delta x}{\Delta y}(\phi_{i,n}^u - \phi_i^u)\alpha_i^u + \sum_{i=0}^{m^u} \frac{\mu_S \Delta x}{\Delta y}(\phi_{i,s}^u - \phi_i^u)\alpha_i^u \\
&+ S^u - \Delta y \frac{RT}{M_w} \sum_{i=0}^{m^\rho} (\phi_{i,E}^\rho - \phi_{i,W}^\rho)\alpha_i^\rho, \qquad (51)
\end{aligned}$$

$$\begin{aligned}
\rho_p^o \Delta V \cdot \sum_{i=1}^{m^v} \dot{\alpha}_i^v \phi_i^v &= -\sum_{i=0}^{m^\rho}\sum_{j=0}^{m^u}\sum_{k=0}^{m^v} \xi_E^v \phi_{i,e}^\rho \phi_{j,E}^u (\phi_{k,e}^v - \phi_k^v)\Delta y \alpha_i^\rho \alpha_j^u \alpha_k^v \\
&+ \sum_{i=0}^{m^\rho}\sum_{j=0}^{m^u}\sum_{k=0}^{m^v} \bar{\xi}_W^v \phi_{i,w}^\rho \phi_{j,W}^u (\phi_{k,w}^v - \phi_k^v)\Delta y \alpha_i^\rho \alpha_j^u \alpha_k^v \\
&- \sum_{i=0}^{m^\rho}\sum_{j=0}^{m^v}\sum_{k=0}^{m^v} \xi_N^v \phi_{i,n}^\rho \phi_{j,N}^v (\phi_{k,n}^v - \phi_k^v)\Delta x \alpha_i^p \alpha_j^v \alpha_k^v \\
&+ \sum_{i=0}^{m^\rho}\sum_{j=0}^{m^v}\sum_{k=0}^{m^v} \bar{\xi}_S^v \phi_{i,s}^\rho \phi_{j,S}^v (\phi_{k,s}^v - \phi_k^v)\Delta x \alpha_i^\rho \alpha_j^v \alpha_k^v \\
&+ \sum_{i=0}^{m^v} \frac{\mu_E \Delta y}{\Delta x}(\phi_{i,e}^v - \phi_i^v)\alpha_i^v + \sum_{i=0}^{m^v} \frac{\mu_W \Delta y}{\Delta x}(\phi_{i,w}^v - \phi_i^v)\alpha_i^v \\
&+ \sum_{i=0}^{m^v} \frac{\mu_N \Delta x}{\Delta y}(\phi_{i,n}^v - \phi_i^v)\alpha_i^v + \sum_{i=0}^{m^v} \frac{\mu_S \Delta x}{\Delta y}(\phi_{i,s}^v - \phi_i^v)\alpha_i^v \\
&+ S^v - g\Delta V \sum_{i=0}^{m^\rho} \phi_i^\rho \alpha_i^\rho - \Delta x \frac{RT}{M_w} \sum_{i=0}^{m^\rho} (\phi_{i,N}^\rho - \phi_{i,S}^\rho)\alpha_i^\rho. \qquad (52)
\end{aligned}$$

By projecting (51) onto the basis function ϕ_l^u, $l \in [1, m^u]$ one obtains m^u ODEs

$$\begin{aligned}\check{\mathcal{A}}_{ll}^u \dot{\alpha}_l^u &= \sum_{i=0}^{m^\rho}\sum_{j=0}^{m^u}\sum_{k=0}^{m^u} \check{\mathcal{F}}_{lijk}^u \alpha_i^\rho \alpha_j^u \alpha_k^u + \sum_{i=0}^{m^\rho}\sum_{j=0}^{m^u}\sum_{k=0}^{m^v} \check{\mathcal{G}}_{lijk}^u \alpha_i^\rho \alpha_j^u \alpha_k^v + \\ &+ \sum_{i=0}^{m^u} \check{\mathcal{H}}_{li}^u \alpha_i^u + \sum_{i=0}^{m^\rho} \check{\mathcal{P}}_{li}^u \alpha_i^\rho + \check{\mathcal{S}}_l^u, \end{aligned} \tag{53}$$

where

$$\check{\mathcal{A}}_{ij}^u = \delta_{ij} \cdot \left(\rho_p^o \phi_j^u \Delta V,\ \phi_i^u\right),$$

$$\check{\mathcal{F}}_{lijk}^u = \left([-\xi_E^u \phi_{i,e}^\rho \phi_{k,E}^u (\phi_{j,e}^u - \phi_j^u)\Delta y + \bar{\xi}_W^u \phi_{i,w}^\rho \phi_{k,W}^u (\phi_{j,w}^u - \phi_j^u)\Delta y],\ \phi_l^u\right),$$

$$\check{\mathcal{G}}_{lijk}^u = \left([-\xi_N^u \phi_{i,n}^\rho \phi_{k,N}^v (\phi_{j,n}^u - \phi_j^u)\Delta x + \bar{\xi}_S^u \phi_{i,s}^\rho \phi_{k,S}^v (\phi_{j,s}^u - \phi_j^u)\Delta x],\ \phi_l^u\right),$$

$$\begin{aligned}\check{\mathcal{H}}_{li}^u &= \left(\frac{\mu_E \Delta y}{\Delta x}(\phi_{i,e}^u - \phi_i^u),\ \phi_l^u\right) + \left(\frac{\mu_W \Delta y}{\Delta x}(\phi_{i,w}^u - \phi_i^u),\ \phi_l^u\right) \\ &+ \left(\frac{\mu_N \Delta x}{\Delta y}(\phi_{i,n}^u - \phi_i^u),\ \phi_l^u\right) + \left(\frac{\mu_S \Delta x}{\Delta y}(\phi_{i,s}^u - \phi_i^u),\ \phi_l^u\right),\end{aligned}$$

$$\check{\mathcal{P}}_{li}^u = -\frac{RT}{M_w}\Delta y \left((\phi_{i,E}^\rho - \phi_{i,W}^\rho),\ \phi_l^u\right),$$

$$\check{\mathcal{S}}_l^u = \left(S^u,\ \phi_l^u\right).$$

By projecting (52) onto the basis function ϕ_l^v, $l \in [1, m^v]$ one obtains m^v ODEs

$$\begin{aligned}\check{\mathcal{A}}_{ll}^v \dot{\alpha}_l^v &= \sum_{i=0}^{m^\rho}\sum_{j=0}^{m^u}\sum_{k=0}^{m^v} \check{\mathcal{F}}_{lijk}^v \alpha_i^\rho \alpha_j^u \alpha_k^v + \sum_{i=0}^{m^\rho}\sum_{j=0}^{m^v}\sum_{k=0}^{m^v} \check{\mathcal{G}}_{lijk}^v \alpha_i^\rho \alpha_j^v \alpha_k^v + \\ &+ \sum_{i=0}^{m^v} \check{\mathcal{H}}_{li}^v \alpha_i^v + \sum_{i=0}^{m^\rho} \check{\mathcal{P}}_{li}^v \alpha_i^\rho + \sum_{i=0}^{m^\rho} \check{\mathcal{M}}_{li}^v \alpha_i^\rho + \check{\mathcal{S}}_l^v, \end{aligned} \tag{54}$$

where

$$\check{\mathcal{A}}_{ij}^v = \delta_{ij} \cdot \left(\rho_p^o \phi_j^v \Delta V,\ \phi_i^v\right),$$

$$\check{\mathcal{F}}_{lijk}^v = \left([-\xi_E^v \phi_{i,e}^\rho \phi_{j,E}^u (\phi_{k,e}^v - \phi_k^v)\Delta y + \bar{\xi}_W^v \phi_{i,w}^\rho \phi_{j,W}^u (\phi_{k,w}^v - \phi_k^v)\Delta y],\ \phi_l^u\right),$$

$$\check{\mathcal{G}}_{lijk}^u = \left([-\xi_N^v \phi_{i,n}^\rho \phi_{j,N}^v (\phi_{k,n}^v - \phi_k^v)\Delta x + \bar{\xi}_S^v \phi_{i,s}^\rho \phi_{j,S}^v (\phi_{k,s}^v - \phi_k^v)\Delta x],\ \phi_l^v\right),$$

$$\begin{aligned}\check{\mathcal{H}}_{li}^u &= \left(\frac{\mu_E \Delta y}{\Delta x}(\phi_{i,e}^v - \phi_i^v),\ \phi_l^v\right) + \left(\frac{\mu_W \Delta y}{\Delta x}(\phi_{i,w}^v - \phi_i^v),\ \phi_l^v\right) \\ &+ \left(\frac{\mu_N \Delta x}{\Delta y}(\phi_{i,n}^v - \phi_i^v),\ \phi_l^v\right) + \left(\frac{\mu_S \Delta x}{\Delta y}(\phi_{i,s}^v - \phi_i^v),\ \phi_l^v\right),\end{aligned}$$

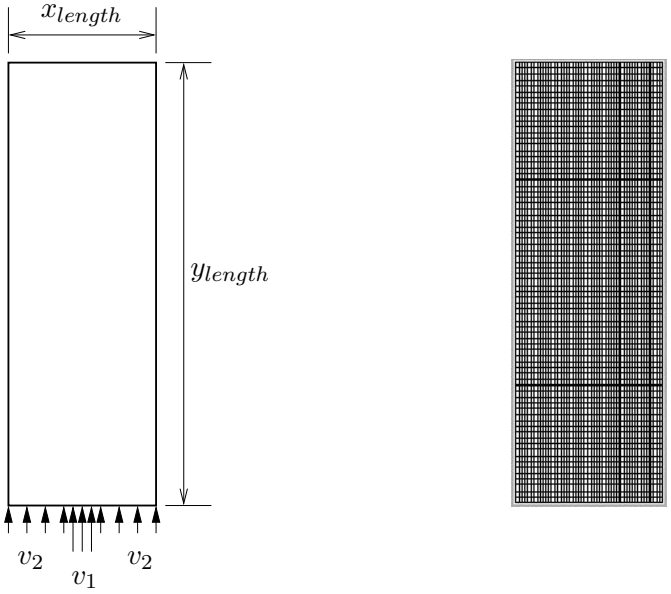
$$\check{\mathcal{P}}_{li}^{v} = -\frac{RT}{M_w}\Delta x\left((\phi_{i,N}^{\rho} - \phi_{i,S}^{\rho}),\ \phi_l^v\right),$$

$$\check{\mathcal{M}}_{li}^{v} = -g\Delta V\left(\phi_i^{\rho},\ \phi_l^v\right),$$

$$\check{\mathcal{S}}_{l}^{v} = \left(S^v,\ \phi_l^v\right).$$

The ODEx3 model has m^ρ ODEs (26), m^u ODEs (53), and m^v ODEs (54). The input data of ODEx3 are the basis functions of ρ, u, and v. The solutions of ODEx3 are α_i^ρ, $i \in [1, m^\rho]$, α_i^u, $i \in [1, m^u]$, and α_i^v, $i \in [1, m^v]$. An example of the input file of ODEx3 is presented in Appendix B.

4.4.1.3 Results for compressible, gas-only flows This section presents the POD-based ROM that was developed for a compressible, gas-only flow case. This case will be called herein case G. The geometry of case G is identical to the geometry of case I. The geometry and boundary conditions of case G are shown in Figure 23(a). Figure 23(b) shows the uniform computational grid used in case G. The parameters of case G are listed in Table 3. Note that MFIX uses CGS units



(a) Geometry and boundary conditions

(b) Computational grid

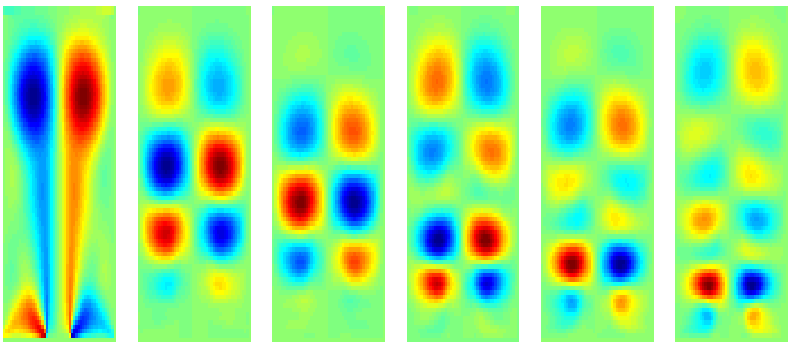
Figure 23: Case G: geometry, boundary conditions, and computational grid

and dimensional variables.

The flow in case G was simulated from $t = 0s$ to $t = 13s$ using MFIX. Snapshots were stored every $0.05s$. Thus 260 snapshots were stored in the database generated by MFIX. POD basis functions of u, v, and p were calculated using the PODDEC package, developed in section 4.2. Figures 24, 25, and 26 show the first six basis functions of u, v, and p, respectively. Figure 27 shows the cumulative energy retained by different number of POD modes.

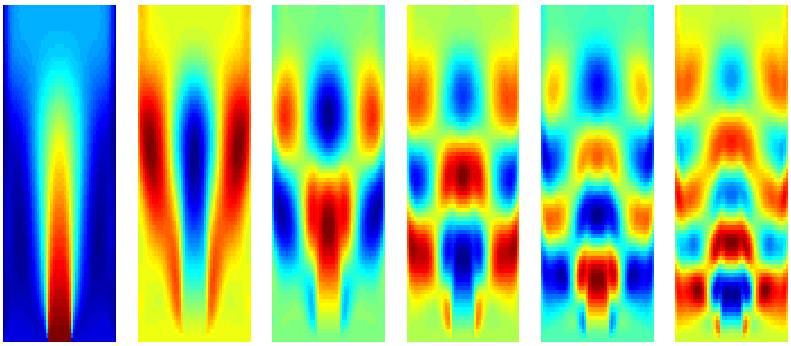
Table 3: Parameters of case G

Parameter	Description	Value
x_{length}	Length of the domain in x-direction	$25.4cm$
y_{length}	Length of the domain in y-direction	$76.5cm$
$imax$	Number of cells in x-direction	50
$jmax$	Number of cells in y-direction	76
v_1, v_2	Gas inflow velocities	$12.6cm/s$, $1.0cm/s$
p_s	Static pressure at outlet	$1.01 \times 10^6 g/(cm \cdot s^2)$
T_0	Gas temperature	$297K$
μ_0	Gas viscosity	$1.8 \times 10^{-4} g/(cm \cdot s)$
t_{start}	Start time	$0s$
t_{stop}	Stop time	$13s$



ϕ_0^u ϕ_1^u ϕ_2^u ϕ_3^u ϕ_4^u ϕ_5^u

Figure 24: Case G: the first six basis functions of u



ϕ_0^v ϕ_1^v ϕ_2^v ϕ_3^v ϕ_4^v ϕ_5^v

Figure 25: Case G: the first six basis functions of v

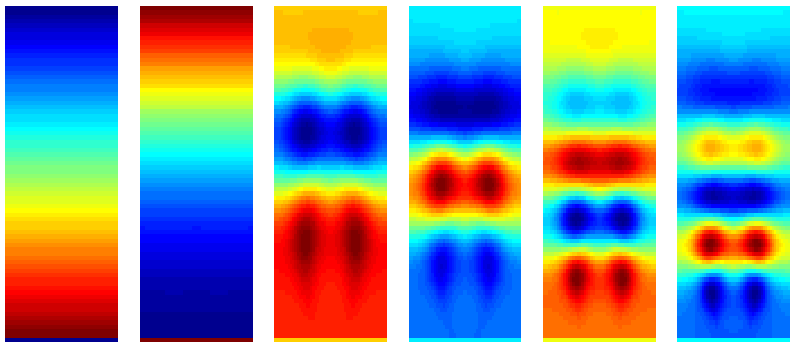
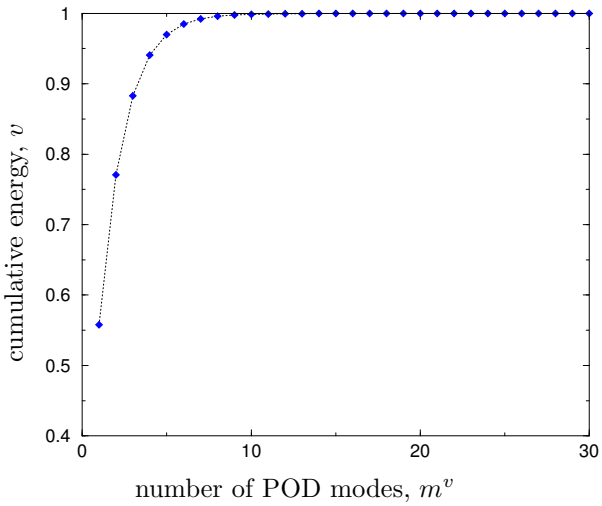
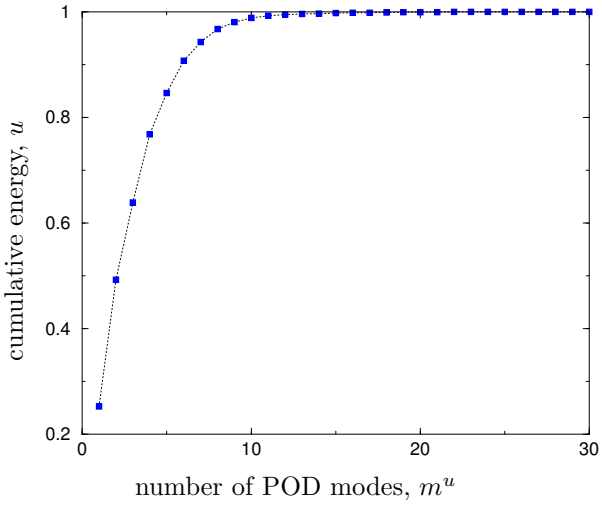


Figure 26: Case G: the first six basis functions of p





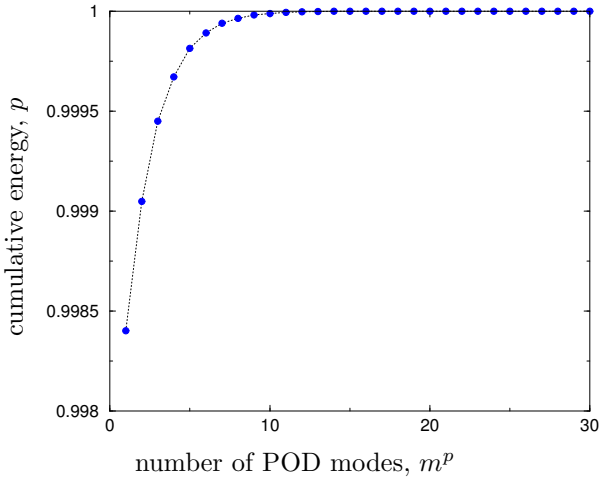


Figure 27: Case G: cumulative energy

4.4.1.3.1 Results at reference condition Let us apply ODExMFIX to the flow of case G at reference condition. Figures 28, 29, and 30 show the first four time coefficients of u, v, and p obtained from ODExMFIX using different number of POD modes. In these figures, the reference time coefficients were obtained by directly projecting the snapshots generated by MFIX onto the POD basis functions. ODExMFIX(2+19+11) denotes the model of ODExMFIX with $m^p = 2$, $m^u = 19$, and $m^v = 11$.

As shown in Figures 28 and 29, by increasing the number of POD modes used by ODExMFIX from (2, 19, 11) to (15, 30, 20) significantly improved the accuracy of the time coefficients of u and v. The time coefficients of u and v predicted by ODExMFIX(15+30+20) agreed very well with the reference time coefficients. By using this number of POD modes, approximately 99.99% of the total energy was retained by the POD modes used in ODExMFIX.

Figure 30 shows that pressure time coefficients predicted by ODExMFIX have large oscillations for $t < 3s$. For $t > 3s$, the pressure time coefficients obtained using (15, 30, 20) POD modes agreed well with the reference time coefficients. It was assumed that the large oscillations of pressure time coefficients was caused by an insufficient number of snapshots in the database. To verify this assumption, the number of snapshots was increased by storing snapshots every $0.01s$ instead of every $0.05s$. Thus the number of snapshots increased from 260 to 1195.

Figure 31 shows the pressure time coefficient, α_1^p, predicted by ODExMFIX(15+30+20) using these two sets of snapshots. Figure 31 shows that increasing the number of snapshots in the database did not improve the prediction of α_1^p. The average magnitude of ϕ_0^p is 1,010,043.89 and the average magnitude of ϕ_1^p is 0.0143. Thus most of the spatial characteristics of the pressure field are captured by ϕ_0^p. The accuracy of the predictions of ϕ_1^p was deteriorated (1) because ϕ_1^p is approximately 8 orders of magnitude smaller than ϕ_0^p, and (2) because the finite representation of the numbers in the computer.

Figures 32, 33, and 34 show the reconstructed flow fields compared against the results of MFIX at $t = 1.25s$, $t = 7.00s$, and $t = 13.00s$. As shown in Figures 32 and 33, the accuracy of the reconstructed u and v using time coefficients obtained from ODExMFIX increased as the number of POD modes used in ODExMFIX increased. Because ϕ_i^p, $i \geq 1$ are at least 8 orders of magnitude smaller than ϕ_0^p, almost all the spatial characteristics of the pressure field are captured by ϕ_0^p. Consequently, the pressure contour plots variation as a function of the number of POD modes is insignificant.

The computational cost for simulating the flow in case G using MFIX was 13,187 seconds of CPU time. The computational cost of ODExMFIX(15+30+20) was 3,352 seconds of CPU time, while for ODExMFIX(6+29+19) was 3,017 seconds and for ODExMFIX(2+19+11) was 1,265 seconds. The computational time of the reduced order model varied between 9.6% and 25.4% of the computational time of MFIX.

ODEx3 was also applied to case G. ODEx3, however, failed to produce a converged result. In ODEx3, the unknowns are α^ρ, α^u, and α^v. The magnitudes of α_1^ρ, α_1^u and α_1^v are of the order of 10^{-10}, 10, and 100, respectively. Compared to u and v, the time coefficients of ρ are too small to be properly captured.

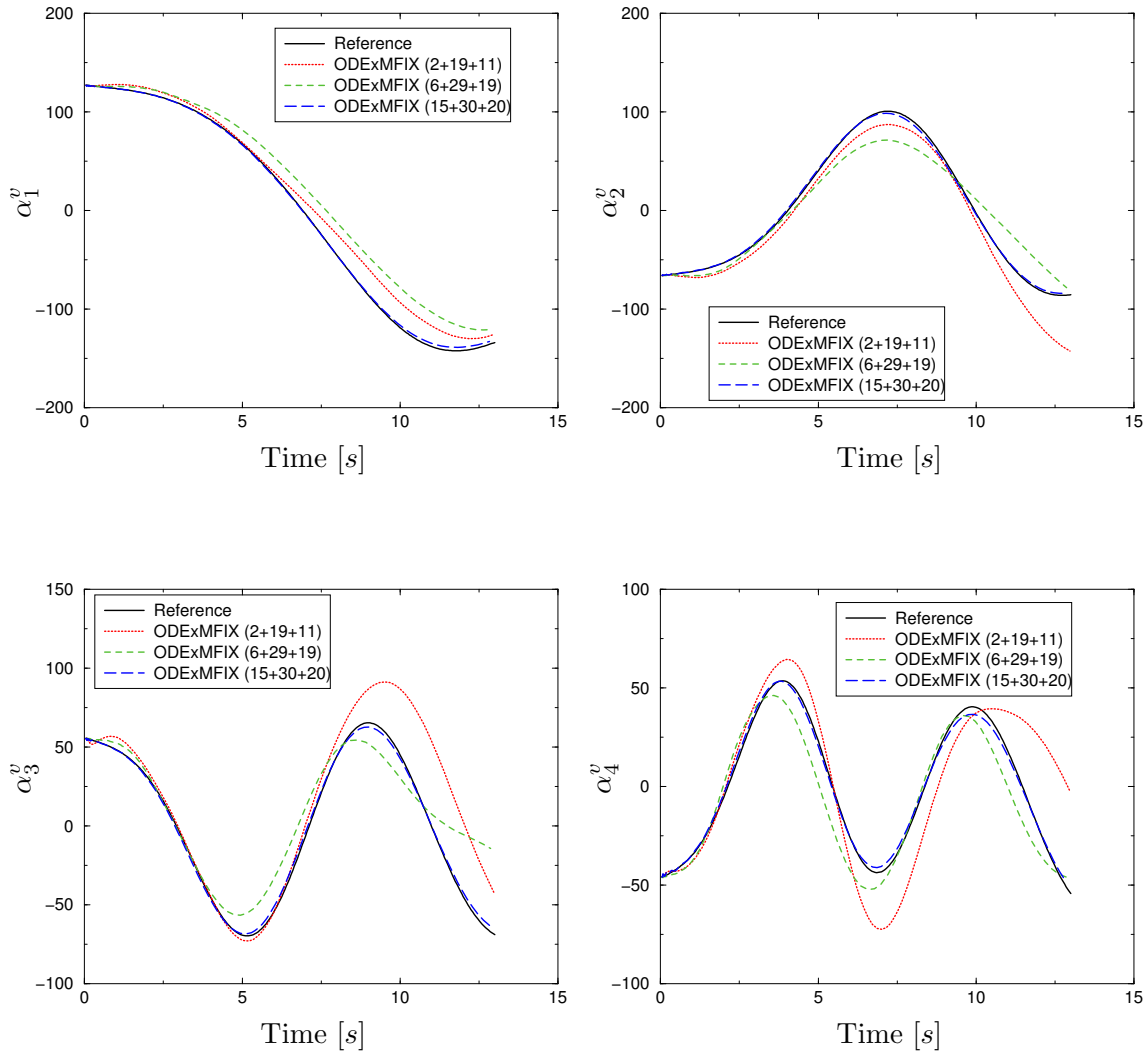


Figure 28: Case G: the first four time coefficients of v

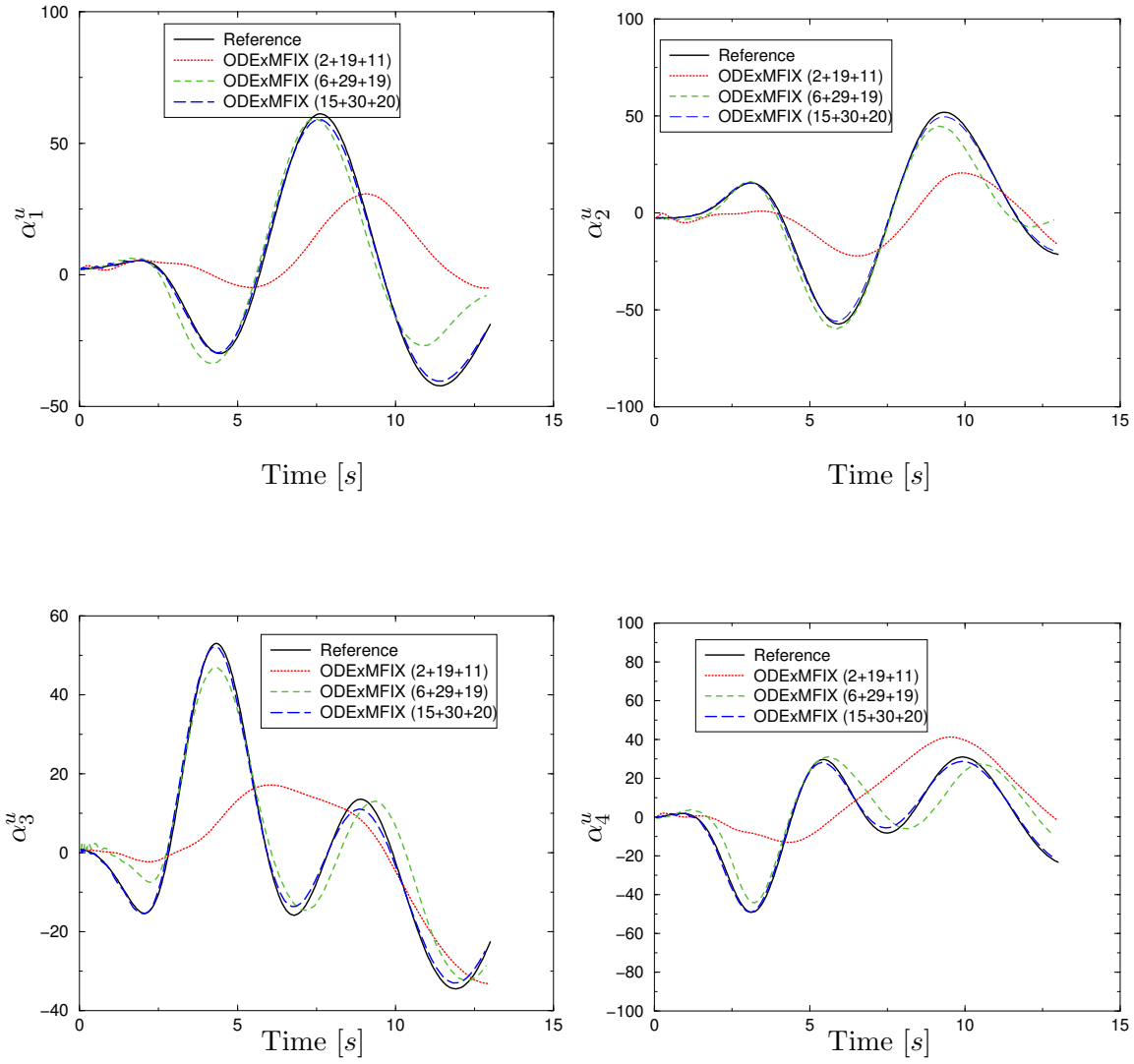


Figure 29: Case G: the first four time coefficients of u

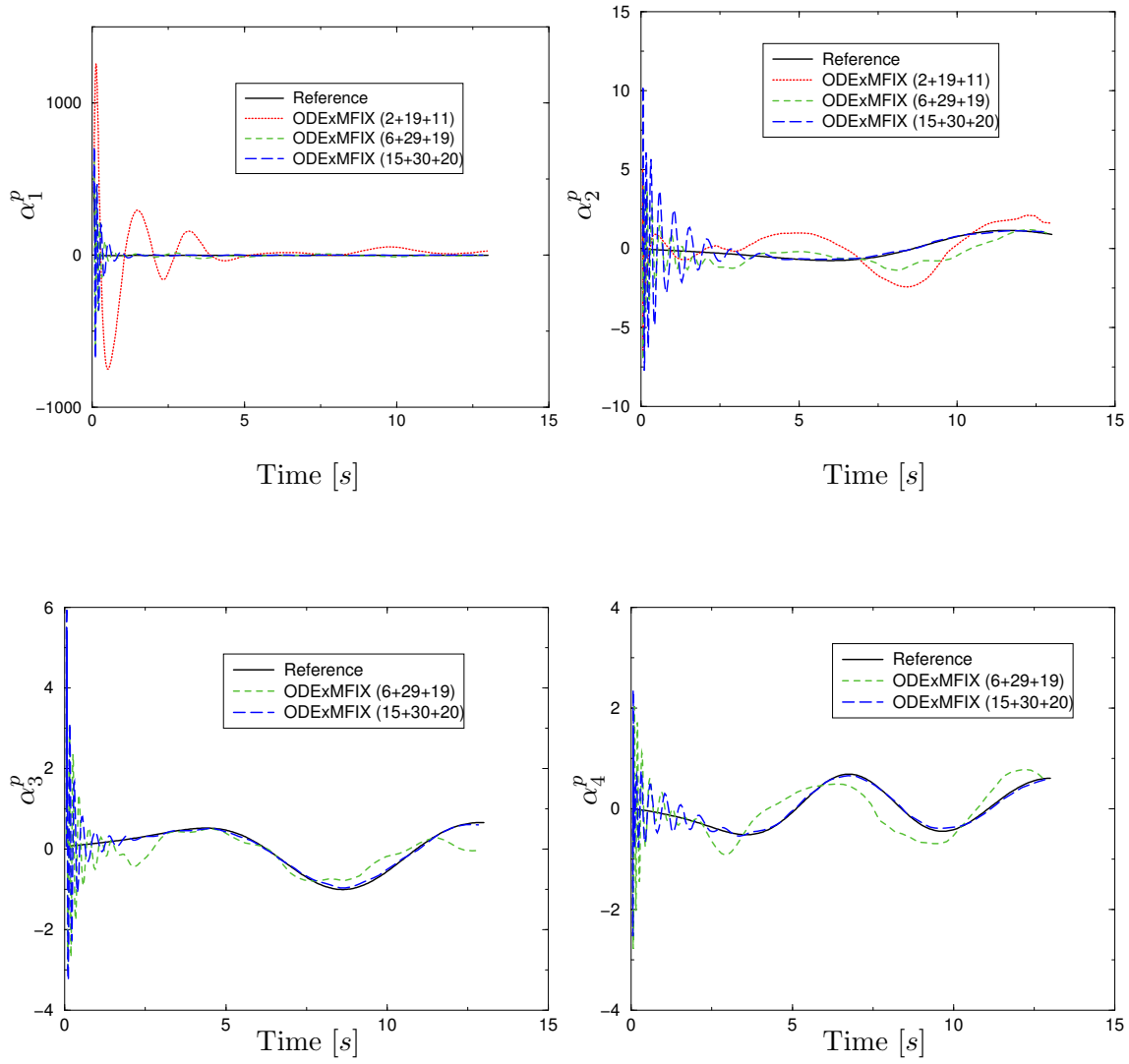


Figure 30: Case G: the first four time coefficients of p

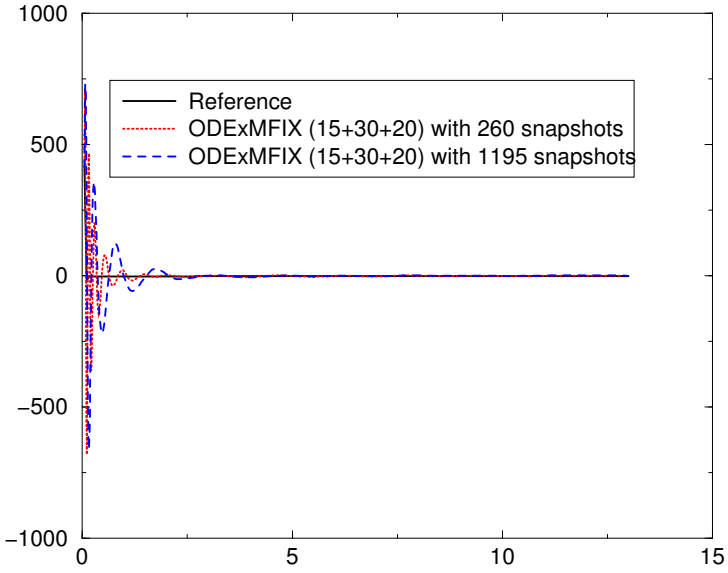
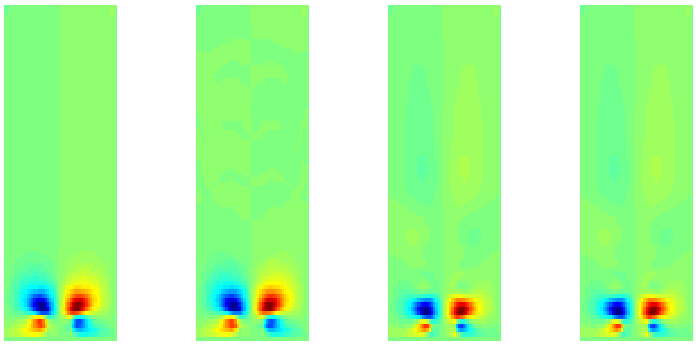
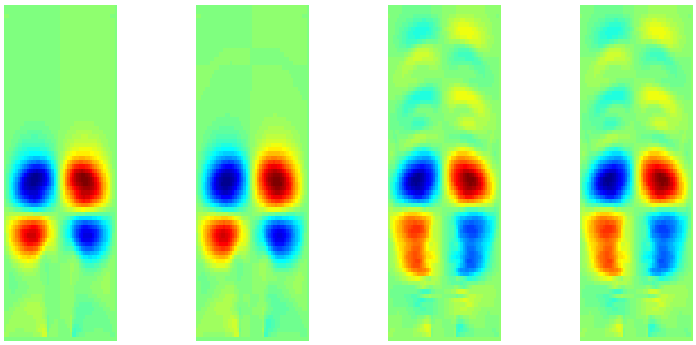


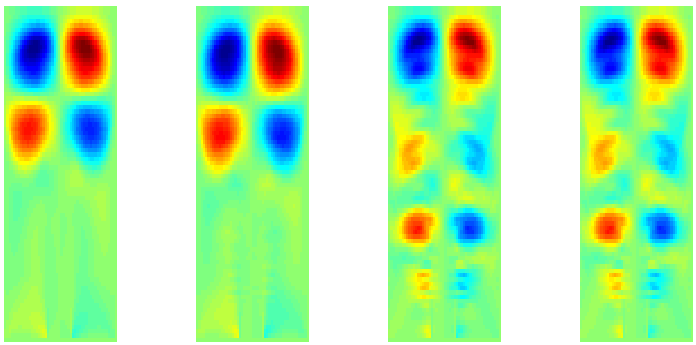
Figure 31: Case G: α_1^p predicted by ODExMFIX using two sets of snapshots



(a) $t = 1.25s$

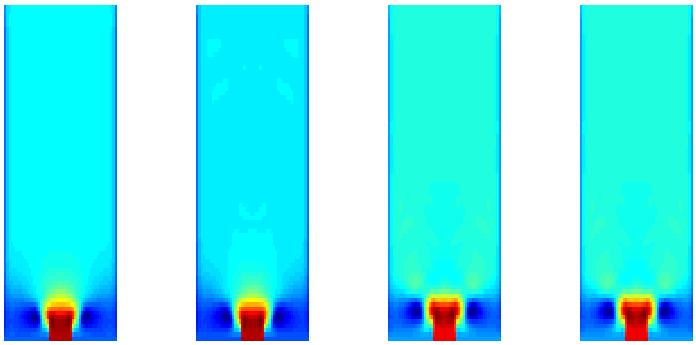


(b) $t = 7.00$



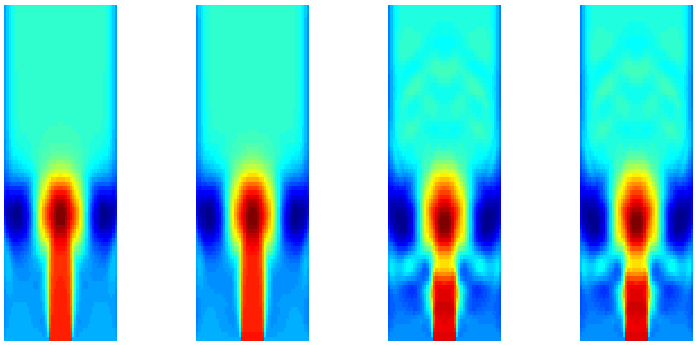
(c) $t = 13.00$

Figure 32: Case G: contour plots of velocity u predicted with MFIX and ODExMFIX



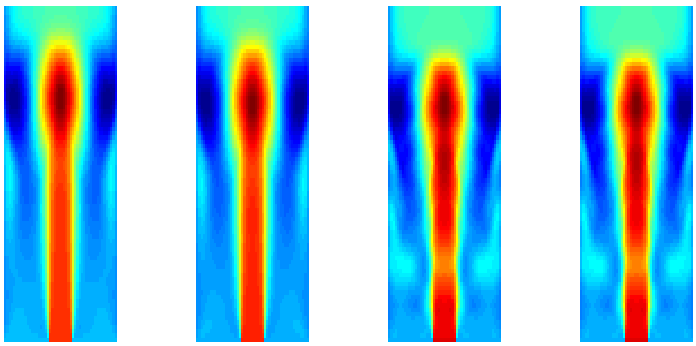
MFIX | ODExMFIX (15+30+20) | ODExMFIX (6+29+19) | ODExMFIX (2+19+11)

(a) $t = 1.25s$



MFIX | ODExMFIX (15+30+20) | ODExMFIX (6+29+19) | ODExMFIX (2+19+11)

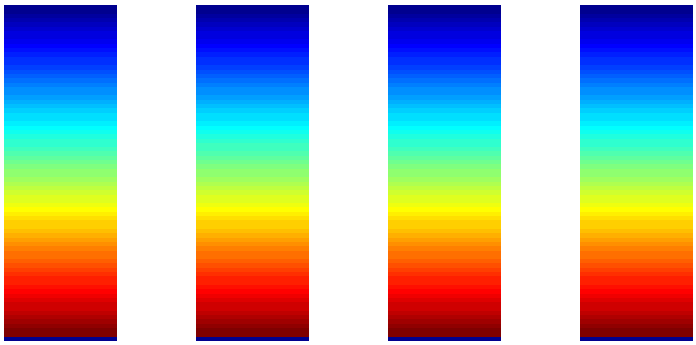
(b) $t = 7.00$



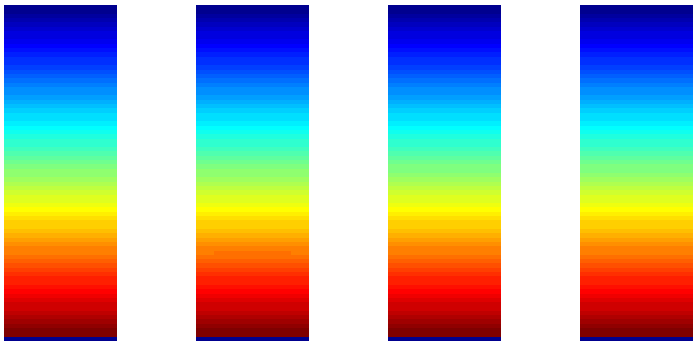
MFIX | ODExMFIX (15+30+20) | ODExMFIX (6+29+19) | ODExMFIX (2+19+11)

(c) $t = 13.00$

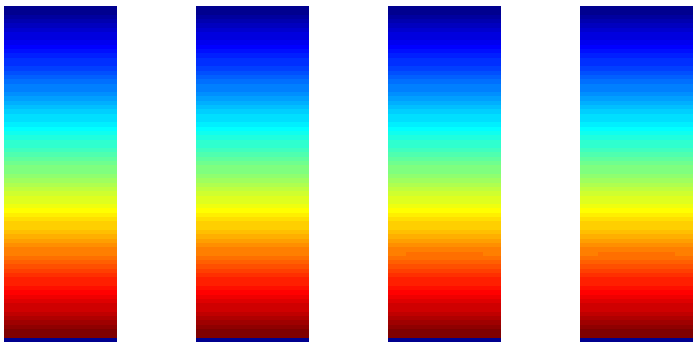
Figure 33: Case G: contour plots of velocity v predicted with MFIX and ODExMFIX



(a) $t = 1.25s$



(b) $t = 7.00$



(c) $t = 13.00$

Figure 34: Case G: contour plots of pressure p predicted with MFIX and ODExMFIX

4.4.1.3.2 Results at off-reference conditions This section investigates the applicability of reduced order models to off-reference conditions. The flow parameter varied was the gas viscosity μ_0. The investigation of the validity of the reduced order model at off-reference conditions was done using case G flow. The reduced order model ODExMFIX was generated using the POD basis functions obtained only at $\mu_0 = 1.8 \times 10^{-4} g/(cm \cdot s)$. In order to measure the accuracy of ODExMFIX at off-reference conditions, MFIX results were obtained *a posteriori*. The error between the full solution MFIX and the reduced order solution ODExMFIX was defined by the error ϵ_{var}

$$\epsilon_{var} = \frac{\sqrt{\sum_{i=1}^{N} (var_i^{MFIX} - var_i^{ROM})^2}}{\sum_{i=1}^{N} |var_i^{MFIX}|}, \tag{55}$$

where var represents the field variables p, u, or v. N is the total number of spatial grid points.

Table 4 lists the errors of ϵ_p, ϵ_u, and ϵ_v at eight different values of μ_0 including the reference value. In Table 4, all the errors were calculated at $t = 13s$. As seen from Table 4, the errors of

Table 4: Case G: errors of ODExMFIX at different values of μ_0

μ_0 $[g/(cm \cdot s)]$	ϵ_p [%]	ϵ_u [%]	ϵ_v [%]
0.8×10^{-4}	3.60×10^{-8}	1.907	0.449
1.0×10^{-4}	3.72×10^{-8}	0.965	0.258
1.1×10^{-4}	3.82×10^{-8}	1.05	0.263
1.3×10^{-4}	2.04×10^{-8}	0.721	0.163
1.5×10^{-4}	5.99×10^{-9}	0.307	0.075
1.6×10^{-4}	7.71×10^{-9}	0.253	0.062
1.8×10^{-4}	1.10×10^{-8}	0.201	0.055
2.0×10^{-4}	8.36×10^{-9}	0.220	0.072
2.2×10^{-4}	1.21×10^{-8}	0.232	0.090
2.4×10^{-4}	2.21×10^{-8}	0.230	0.107
2.6×10^{-4}	1.54×10^{-8}	0.285	0.132
2.8×10^{-4}	3.32×10^{-8}	0.320	0.148
3.0×10^{-4}	3.07×10^{-8}	0.376	0.166

pressure, ϵ_p, for all the eight conditions are very small, because the speed of the gas flow in case G is very low and the pressure variations are very small. Figure 35 shows the errors of ϵ_u and ϵ_v at different values of μ_0.

As shown in Figure 35, for each viscosity value the error ϵ_v is always smaller than ϵ_u because the flow in case G is mainly along the $y-$direction and it is easier for ODExMFIX to capture the details of v_g than the details of u_g. At reference conditions, $\mu_0 = 1.8 \times 10^{-4} g/(cm \cdot s)$, both errors ϵ_v and ϵ_u have minimum values. Figures 36 and 37 show the variation of the errors as a function of time and viscosity value. For the v_g velocity, the error increases with time. The minimum error always corresponds to $\mu_0 = 1.8 \times 10^{-4} g/(cm \cdot s)$. The errors of the u_g velocity have a less ordered variation because the flow in the x-direction is secondary and the errors are larger.

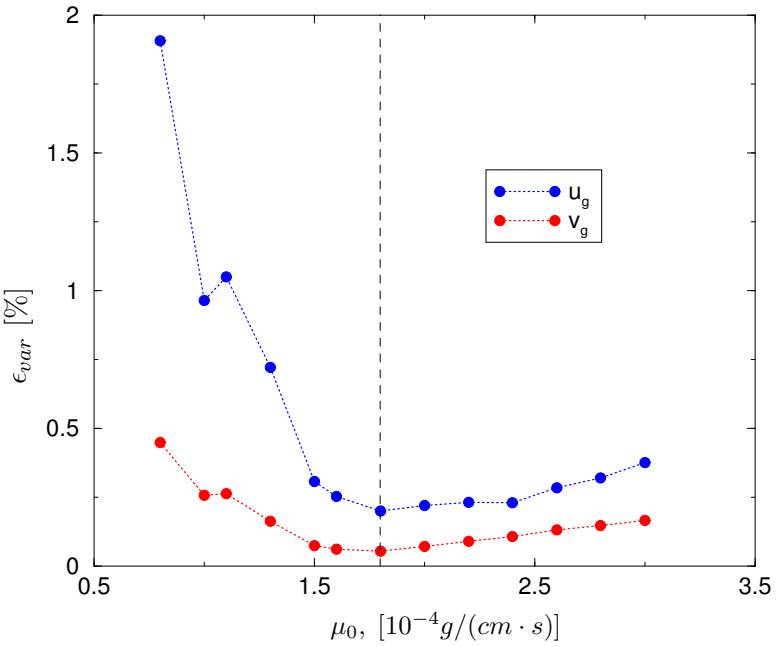


Figure 35: Case G: errors ϵ_u and ϵ_v at time t=13 s for different values of viscosity

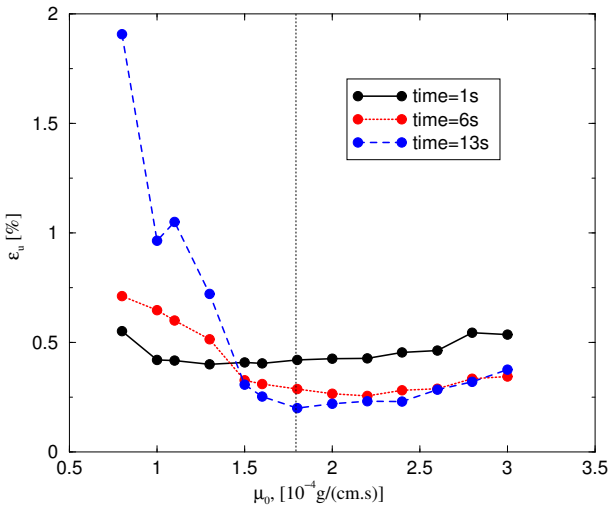


Figure 36: Case G: errors ϵ_u at three time values and for different values of viscosity

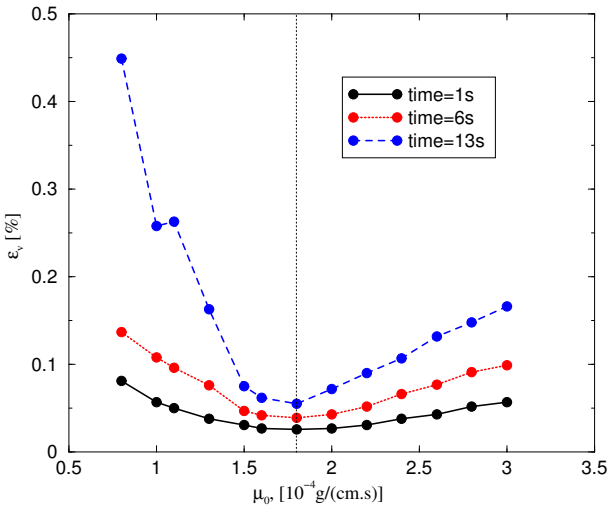


Figure 37: Case G: errors ϵ_v at three time values and for different values of viscosity

As μ_0 increased or decreased from the reference value, both ϵ_v and ϵ_u increased. The errors ϵ_v and ϵ_u increased more rapidly when μ_0 decreased from the reference μ_0 than when μ_0 increased, because smaller μ_0 increased the Reynolds number and generated more complicated flow fields. Figures 38 and 39 show the contour plots of velocities u_g and v_g at $\mu_0 = 0.8 \times 10^{-4} g/(cm \cdot s)$, $1.8 \times 10^{-4} g/(cm \cdot s)$, and $3.0 \times 10^{-4} g/(cm \cdot s)$.

4.4.2 Reduced order model based on proper orthogonal decomposition for gas-solids transport phenomena

For two-dimensional gas-solids transport phenomena, MFIX solves the discretized x-momentum equations of the gas-phase and the solids-phase (3), the discretized y-momentum equations of the gas-phase and the solids-phase (4), the gas pressure correction equation (5), and the solids volume fraction correction equation (56)

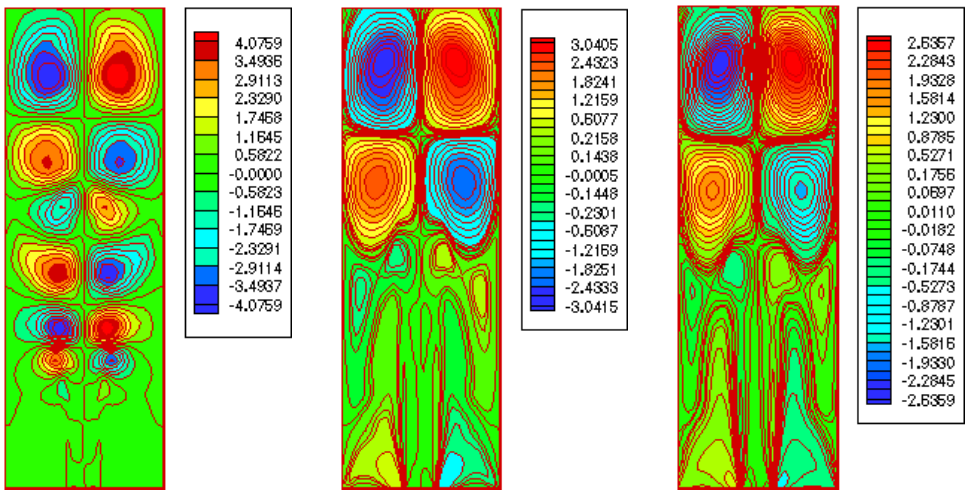
$$a_P^{\epsilon} \epsilon'_{sP} = \sum_{nb} a_{nb}^{\epsilon} \epsilon'_{snb} + b_P^{\epsilon}. \tag{56}$$

The dependent field variables in MFIX are the gas pressure p_g, the void fraction ϵ_g, and the velocity components of the gas-phase and the solids-phase, u_g, v_g, u_s, and v_s.

Let us assume that the database containing a number of snapshots of p_g, ϵ_g, u_g, u_s, v_g, and v_s has been generated and the POD basis functions $\phi_i^{p_g}$, $\phi_i^{u_g}$, $\phi_i^{v_g}$, $\phi_i^{u_s}$, and $\phi_i^{v_s}$ have been extracted from this database. Herein the POD basis functions of ϵ_g are not computed because in MFIX an intermediate variable, the solids volume fraction ϵ_s, is introduced and the solids volume fraction correction equation (56) is used to solve the corrections of ϵ_s. ϵ_g is computed from ϵ_s as

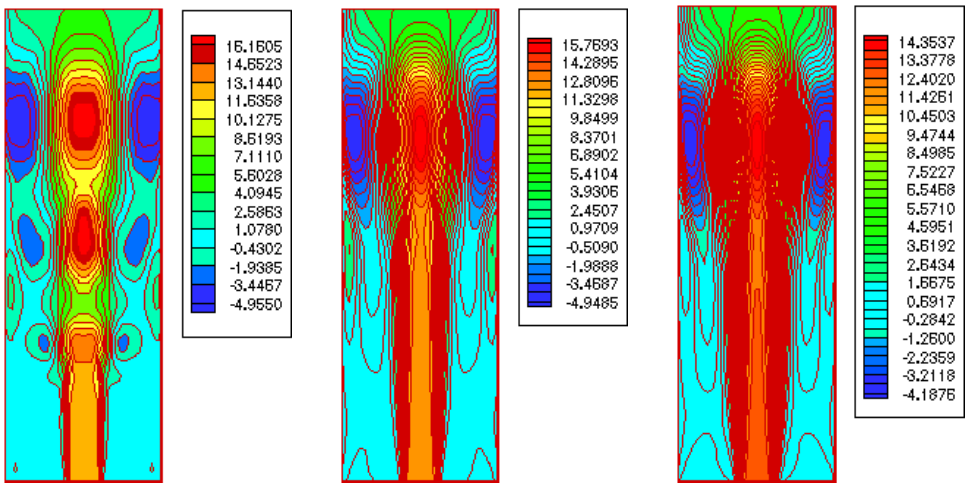
$$\epsilon_g = 1 - \epsilon_s. \tag{57}$$

The code developed for the POD-based ROM of the gas-solids transport phenomena is called ODExS. In ODExS, the solids volume fraction ϵ_s is also introduced as an intermediate variable.



(a) $\mu_0 = 0.8 \times 10^{-4} g/(cm \cdot g)$ (b) $\mu_0 = 1.8 \times 10^{-4} g/(cm \cdot g)$ (c) $\mu_0 = 3.0 \times 10^{-4} g/(cm \cdot g)$

Figure 38: Case G: contour plots of velocity u_g at different values of viscosity



(a) $\mu_0 = 0.8 \times 10^{-4} g/(cm \cdot g)$ (b) $\mu_0 = 1.8 \times 10^{-4} g/(cm \cdot g)$ (c) $\mu_0 = 3.0 \times 10^{-4} g/(cm \cdot g)$

Figure 39: Case G: contour plots of velocity v_g at different values of viscosity

ODExS uses the same solid volume fraction correction equation as used in MFIX. Consequently, ODExS is a *hybrid* model, because the order of the solids volume fraction correction equation has not been reduced. One reason for keeping the correction equation for the solids volume fraction in ODExS is to enforce that void fraction ϵ_g belongs to the interval $[0, 1]$. If ϵ_g were approximated using the POD basis functions of ϕ^{ϵ_g}, it could be possible that at some grid points the reconstructed void fraction values be larger than 1 because of the approximations in the reduced order model.

Using the approach presented for constructing ODExMFIX, the discretized x-momentum equations, the discretized y-momentum equations, and the discretized gas pressure correction equation are projected onto the basis functions ϕ^{u_ℓ}, ϕ^{v_ℓ}, and ϕ^{p_g}, respectively. Herein, ℓ denotes either the gas or solids phase, g or s. Five systems of linear algebraic equations are obtained:

$$\tilde{\mathcal{A}}^{u_\ell}\alpha^{u_\ell} = \tilde{\mathcal{B}}^{u_\ell}, \tag{58}$$

$$\tilde{\mathcal{A}}^{v_\ell}\alpha^{v_\ell} = \tilde{\mathcal{B}}^{v_\ell}, \tag{59}$$

$$\tilde{\mathcal{A}}^{p_g}\alpha^{p_g} = \tilde{\mathcal{B}}^{p_g}, \tag{60}$$

The definitions of $\tilde{\mathcal{A}}$ and $\tilde{\mathcal{B}}$ were presented in section 4.4.1.1.

The input data of ODExS consist of $\phi_i^{p_g}$, $\phi_i^{u_g}$, $\phi_i^{v_g}$, $\phi_i^{u_s}$, $\phi_i^{v_s}$, and the initial field of ϵ_g. The solutions of ODExS, $\alpha_i^{p_g}$, $\alpha_i^{u_g}$, $\alpha_i^{v_g}$, $\alpha_i^{u_s}$, $\alpha_i^{v_s}$ and ϵ_g are calculated iteratively using the following expressions:

$$\alpha_i^{p_g}(t) = (\alpha_i^{p_g})^*(t) + \alpha_i^{p'_g}(t), \tag{61}$$

$$p'_g = \sum_{i=1}^{m_g^p} \alpha_i^{p'_g} \phi_i^{p_g}, \tag{62}$$

$$\alpha_i^{u_m}(t) = (\alpha_i^{u_m})^*(t) + \left(-d_{mp}(p'_{g_E} - p'_g),\ \phi_i^{u_m}\right), \tag{63}$$

$$\alpha_i^{v_m}(t) = (\alpha_i^{v_m})^*(t) + \left(-d_{mp}(p'_{g_N} - p'_g),\ \phi_i^{v_m}\right), \tag{64}$$

where m denotes the phase (g or s). Herein, the superscript $*$ indicates tentative value(*i.e.*, value before correction. The velocity corrections along the x-direction are given by [3]

$$u_{mp} = u^*_{mp} - d_{mp}(p'_{g_E} - p'_{g_W}), \tag{65}$$

where

$$d_{gp} = A_p \left(\epsilon_{g_p} + \frac{\epsilon_{sp} F_{gs} \Delta V}{a^u_{sp} + F_{gs} \Delta V} \right) / \left(a^u_{g_p} + \frac{a^u_{sp} F_{gs} \Delta V}{a^u_{sp} + F_{gs} \Delta V} \right), \tag{66}$$

$$d_{sp} = A_p \left(\epsilon_{sp} + \frac{\epsilon_{g_p} F_{gs} \Delta V}{a^u_{g_p} + F_{gs} \Delta V} \right) / \left(a^u_{sp} + \frac{a^u_{g_p} F_{gs} \Delta V}{a^u_{g_p} + F_{gs} \Delta V} \right). \tag{67}$$

Note that in Equations (65), (66), and (67), p is the control volume center shown in Figure 22(a). Similarly, the velocity corrections along the y-direction are given by

$$v_{mp} = v^*_{mp} - d_{mp}(p'_{g_N} - (p'_g)_S), \tag{68}$$

where p now is the control volume center shown in Figure 22(b).

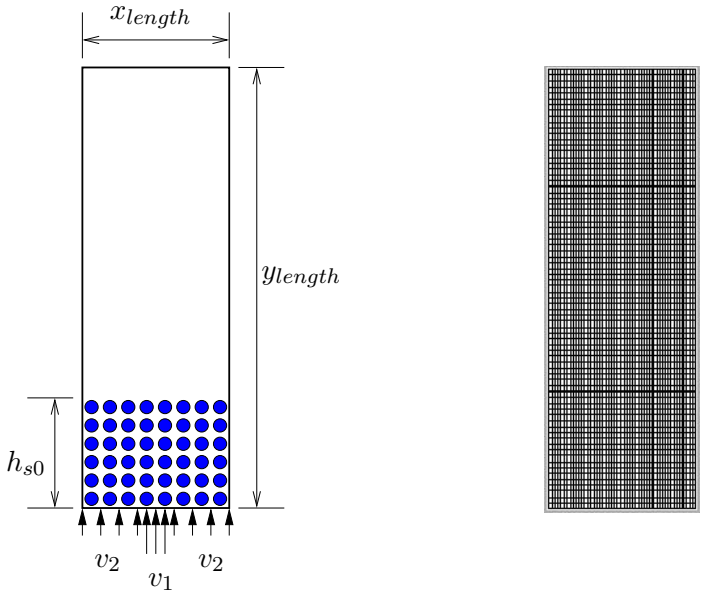
An outline of the solution algorithm in ODExS is described below:

- Using the time coefficients from the previous iteration, reconstruct the field variables p_g, u_g, v_g, u_s, and v_s. Calculate physical properties ρ_g and ρ_s. Calculate transport properties μ_g, μ_s, and F_{gs}.
- Solve the systems of linear algebraic equations (58) and obtain the tentative values of $\alpha_i^{u_g}(t)$, $i \in [1, m^{u_g}]$ and $\alpha_i^{u_s}(t)$, $i \in [1, m^{u_s}]$.
- Solve the systems of linear algebraic equations (59) and obtain the tentative values of $\alpha_i^{v_g}(t)$, $i \in [1, m^{v_g}]$ and $\alpha_i^{v_s}(t)$, $i \in [1, m^{v_s}]$.
- Solve the system of linear equations (60) and obtain $\alpha_i^{p'_g}(t)$, $i \in [1, m^p]$.
- Correct $\alpha_i^{u_g}$, $\alpha_i^{u_s}$, $\alpha_i^{v_g}$, $\alpha_i^{v_s}$, and $\alpha_i^{p_g}$ using equations (61)-(64).

- Solve the solids volume fraction correction equation (56) and obtain $(\epsilon_s)'$. Correct ϵ_s, $\alpha_i^{u_s}$, and $\alpha_i^{v_s}$.
- Calculate the void fraction, ϵ_g, using equation (57).
- Check the convergence. If converged, advance to the next time step.

An example of the input file for ODExS is presented in Appendix C.

4.4.2.1 Results for gas-solids transport phenomena in a fluidized bed Case I presented in section 4.1 was used to test validity of the reduced order model for gas-solids transport phenomena in a fluidized bed. The geometry and boundary conditions of case I are shown in Figure 40(a). Figure 40(b) illustrates the uniform computational grid used in case I. Table 5 lists the parameters



(a) Geometry and boundary conditions

(b) Computational grid

Figure 40: Case I: geometry, boundary conditions, and computational grid

of case I, where ρ_{so}, D_p, h_{s0}, and ϵ_g^* denote the constant solids density, solids particle diameter, initial packed bed height, and packed bed void fraction, respectively.

MFIX was used to simulate the transport phenomena in case I from $t = 0s$ to $t = 1s$. From $t = 0s$ to $t = 0.2s$, the velocities were equal, $v_1 = v_2 = 1cm/s$. At $t = 0.2s$, v_2 was increased to $120.0cm/s$. From $t = 0.2s$ to $t = 1.0s$, snapshots were stored every $0.0025s$. Thus 320 snapshots were stored in the database. POD was then applied to the database to calculate the POD basis functions. Figures 41-45 show the first six POD basis functions of p_g, u_g, v_g, u_s, and v_s, respectively.

Table 6 lists the number of POD modes needed to retain certain portions of the total energy.

Table 5: Parameters of case I

Parameter	Value
x_{length}	$25.4cm$
y_{length}	$76.5cm$
$imax$	50
$jmax$	78
v_1	$120.0cm/s$
v_2	$1.0cm/s$
p_{g_s}	$1.01 \times 10^6 g/(cm \cdot s^2)$
T_{g0}	$297K$
μ_{g0}	$1.8 \times 10^{-4} g/(cm \cdot s)$
t_{start}	$0.2s$
t_{stop}	$1s$
Δt	$1 \times 10^{-4} s$
ρ_{so}	$1.0g/cm^3$
D_p	$0.05cm$
h_{s0}	$14.7cm$
ϵ_g^*	0.4

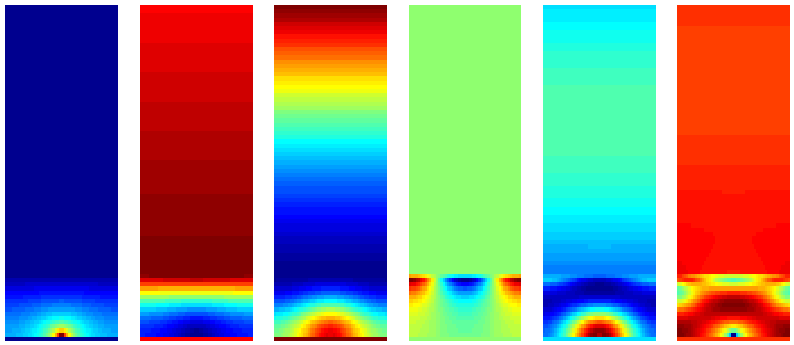


Figure 41: Case I: the first six basis functions of p_g

Table 6: Case I: POD energy vs number of modes for p_g, u_g, v_g, u_s, and v_s

POD	Number of modes				
energy	p_g	u_g	v_g	u_s	v_s
99%	2	4	3	4	2
99.9%	3	7	5	6	3
99.99%	4	11	7	7	5

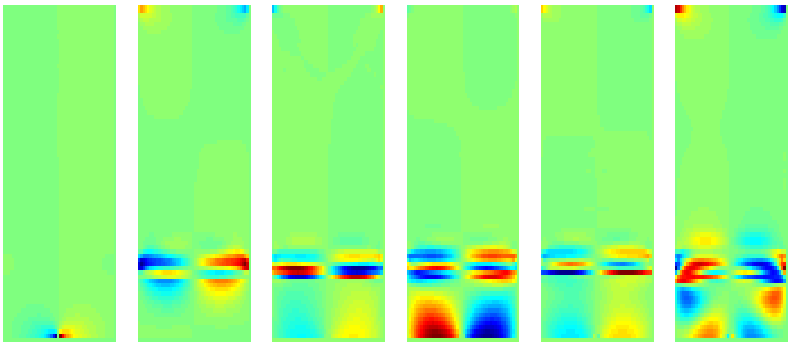


Figure 42: Case I: the first six basis functions of u_g

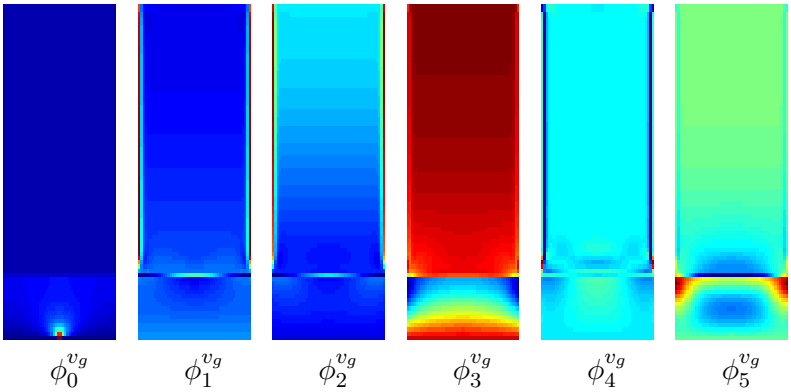


Figure 43: Case I: the first six basis functions of v_g

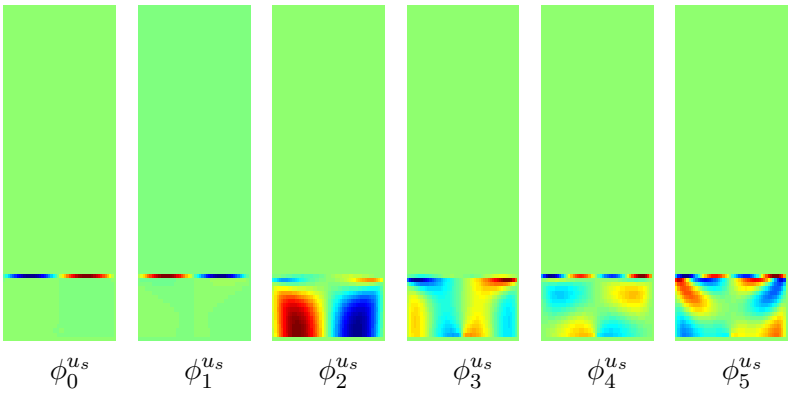


Figure 44: Case I: the first six basis functions of u_s

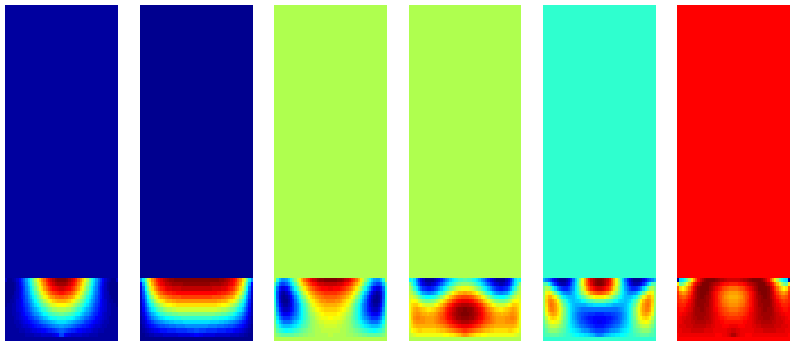


Figure 45: Case I: the first six basis functions of v_s

4.4.2.1.1 Results at reference condition Let us examine the results of ODExS applied to case I at the reference condition. Herein, we chose $m^{p_g} = 4$, $m^{u_g} = 11$, $m^{v_g} = 7$, $m^{u_s} = 7$, and $m^{v_s} = 5$ such that 99.99% of the total energy was retained by the POD modes used in ODExS. The computational cost of using MFIX to simulate the transport phenomena in case I was 23,008 seconds of CPU time. The computational cost of using ODExS with (4, 11, 7, 7, 5) POD modes was 7,595 seconds of CPU time. The cost of ODExS was 33.01% of the cost of MFIX.

Figure 46 compares the first four time coefficients of u_g obtained using ODExS against the time coefficients obtained by direct projection. Figures 47, 48 and 49 show similar results for the time coefficients of v_g, u_s and v_s.

Figures 50-55 show the field variables ϵ_g, p_g, u_g, v_g, u_s and v_s obtained from ODExS compared against the results of MFIX at $t = 1s$. Table 7 lists the errors ϵ_{var} (55) of the field variables obtained at $t = 1s$. Herein var represents ϵ_g, p_g, u_g, u_s, or v_s. As seen from Figures 50-55 and Table 7, the results of ODExS agree very well with the results of MFIX at the reference condition.

Table 7: Case I: ODExS errors at reference condition

Variable	Error, ϵ_{var} [%]
ϵ_g	0.0000356
p_g	0.000000578
u_g	0.01035
v_g	0.01026
u_s	0.505
v_s	0.765

4.4.2.1.2 Results at off-reference conditions This section investigates the accuracy of the reduced order model at off-reference conditions, that is, when one or more parameters of the transport equations are different from the value(s) used for the database generation. The parameter investigated in this section is the solid particle diameter, D_p. The database was generated by

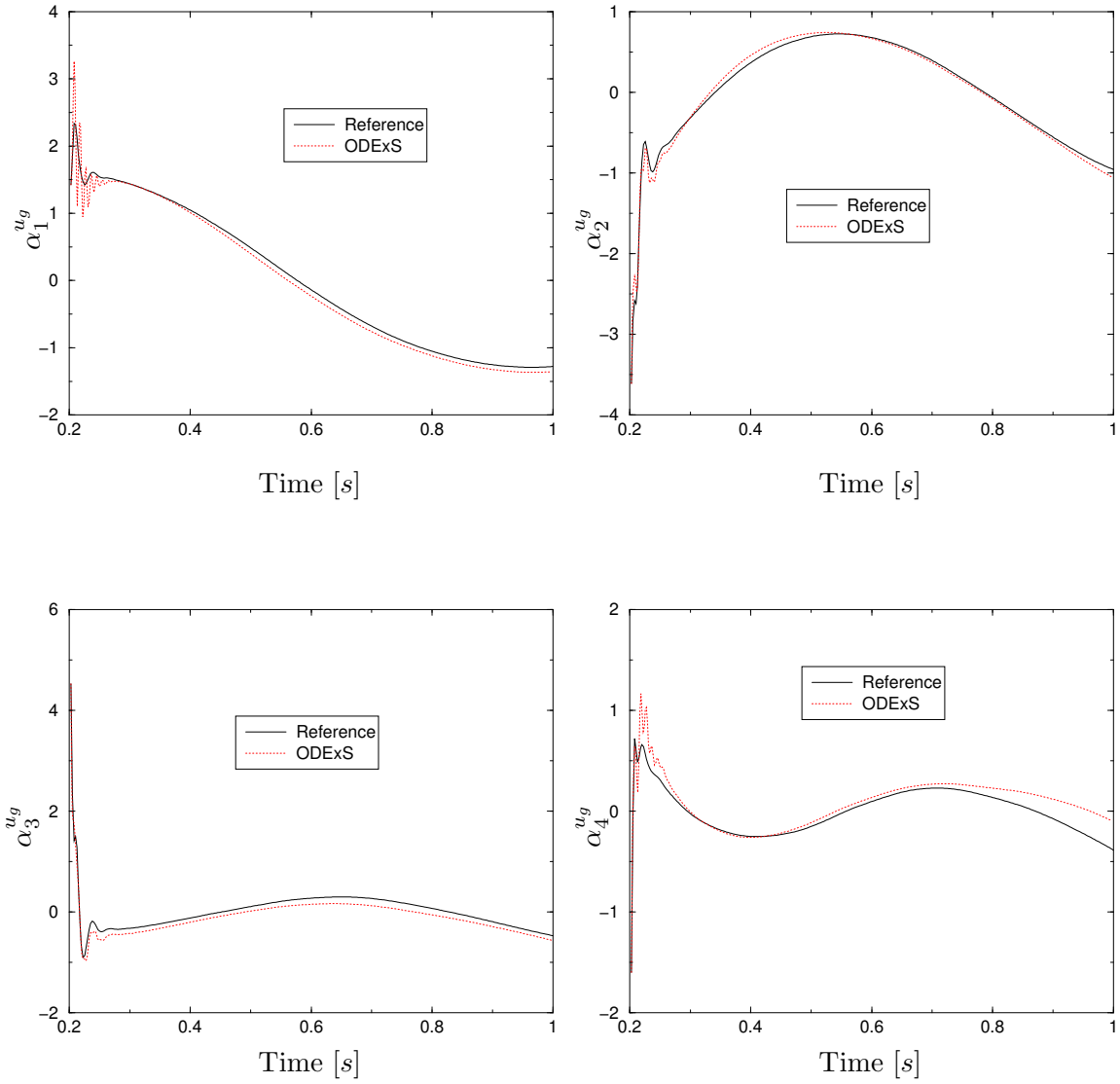


Figure 46: Case I: the first four time coefficients of u_g obtained from ODExS

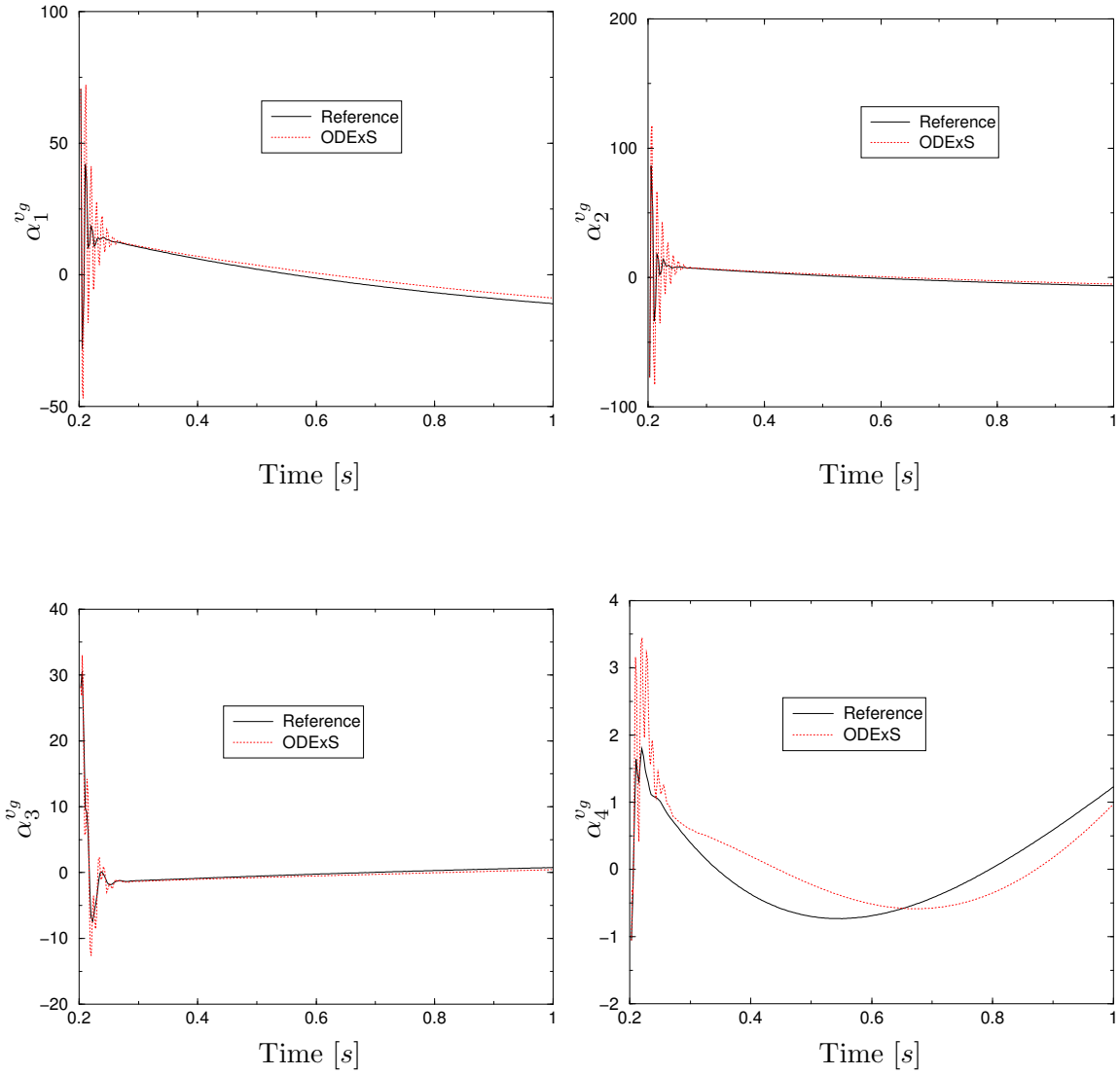


Figure 47: Case I: the first four time coefficients of v_g obtained from ODExS

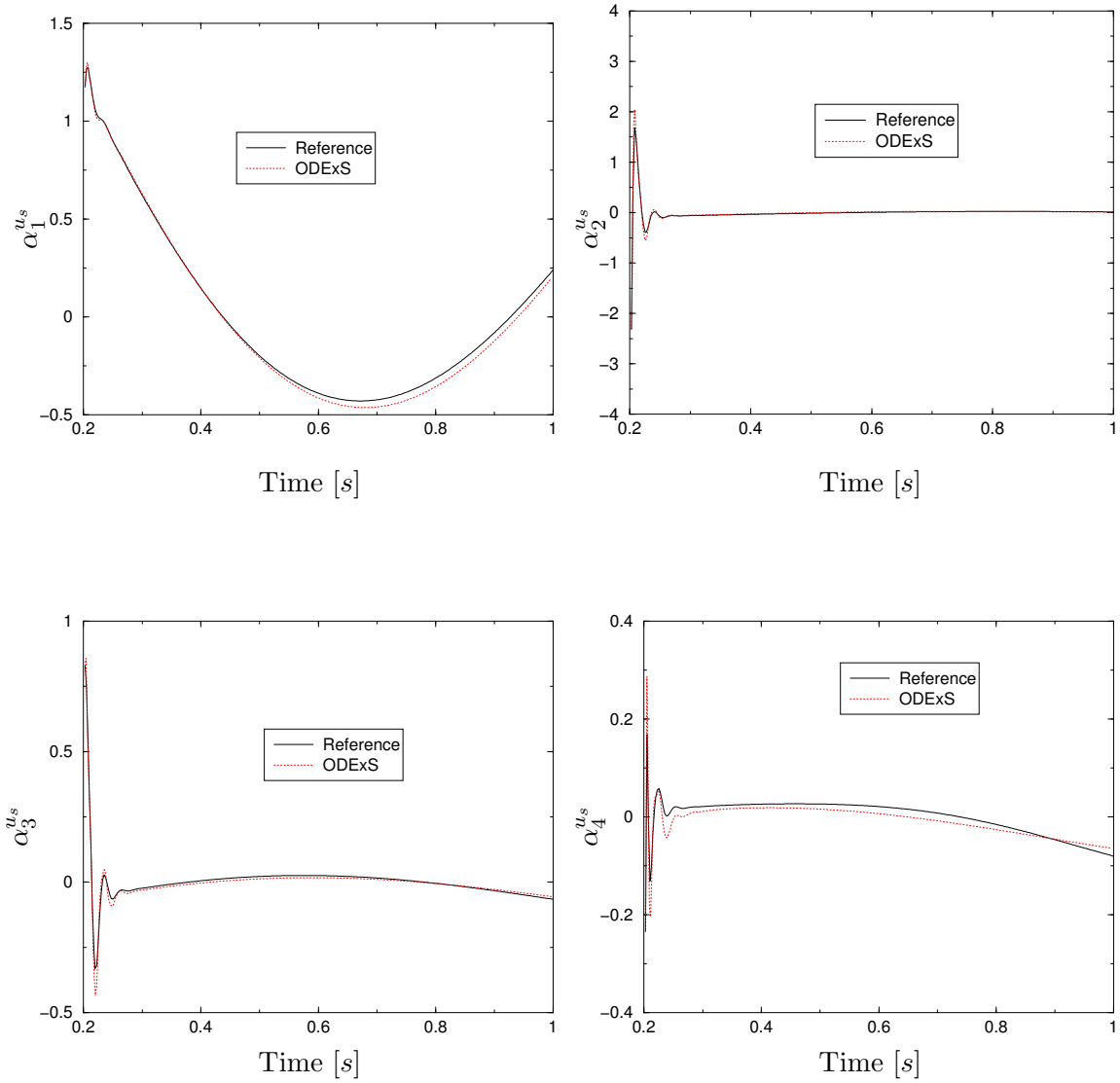


Figure 48: Case I: the first four time coefficients of u_s obtained from ODExS

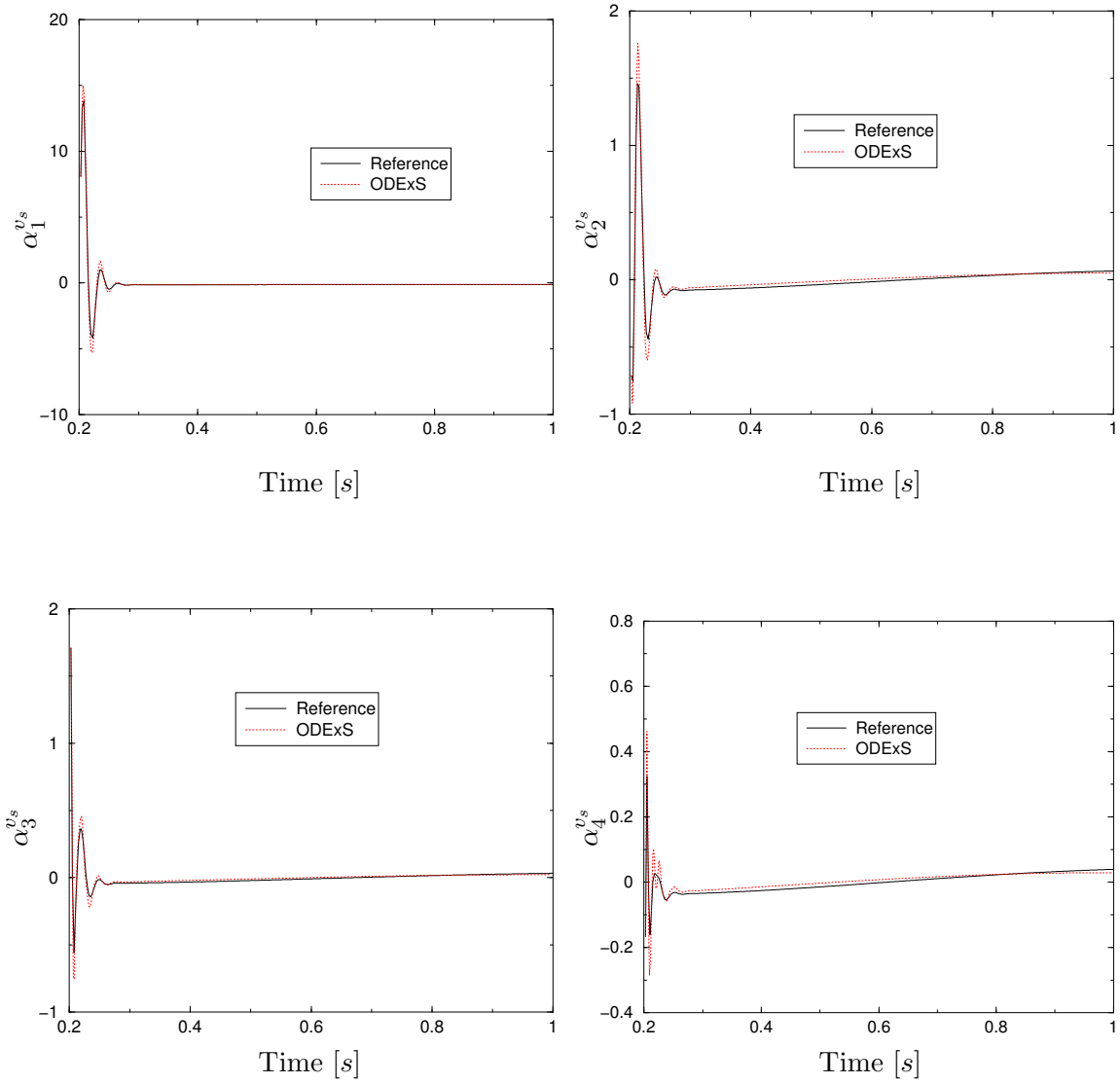
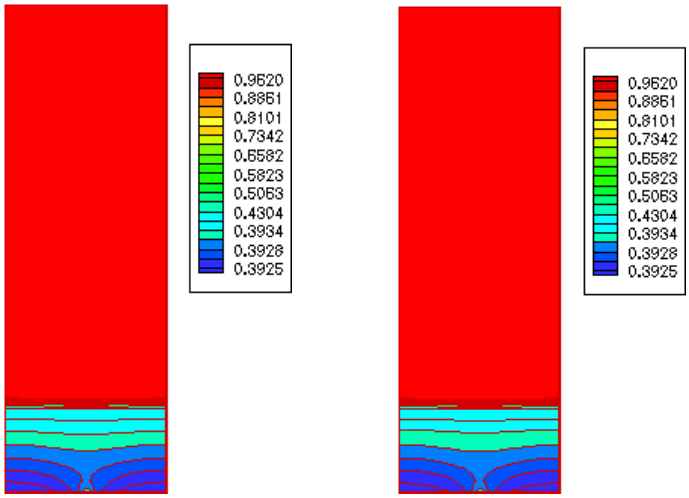
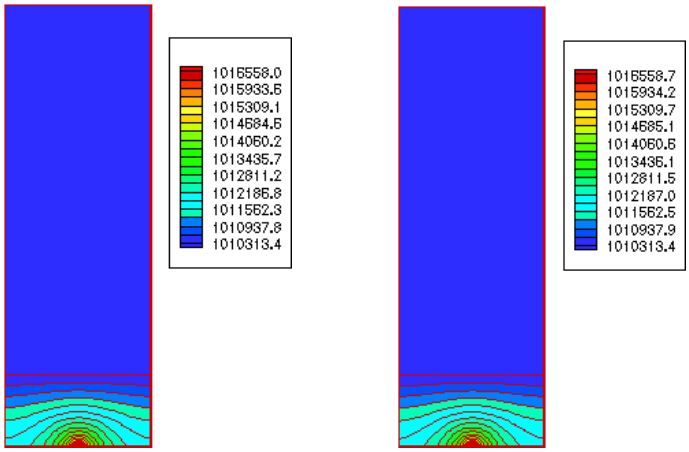


Figure 49: Case I: the first four time coefficients of v_s obtained from ODExS



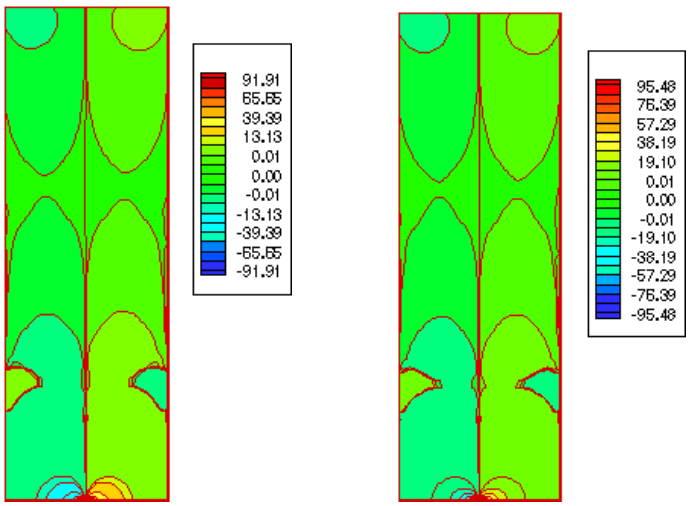
(a) MFIX (b) ODExS

Figure 50: Case I: ϵ_g at $t = 1s$



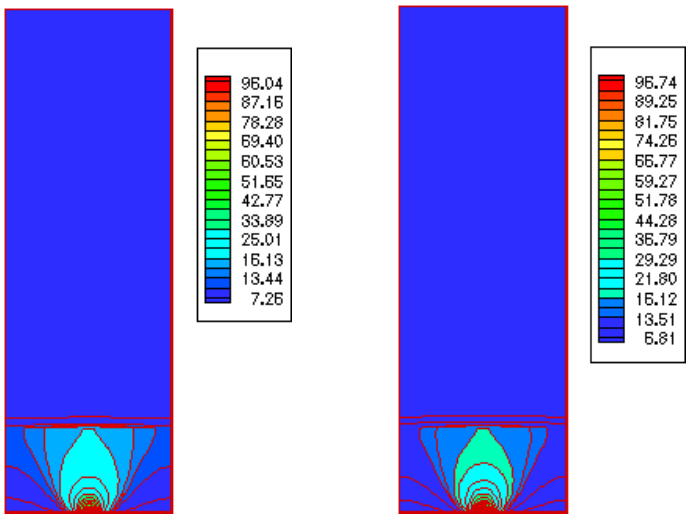
(a) MFIX (b) ODExS

Figure 51: Case I: p_g at $t = 1s$



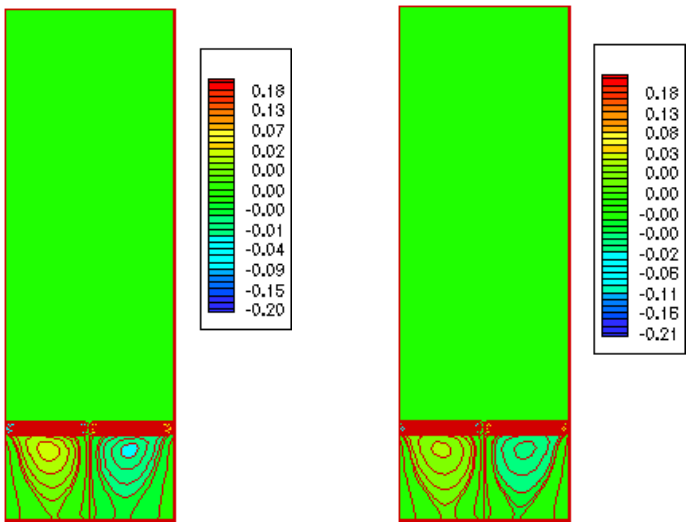
(a) MFIX (b) ODExS

Figure 52: Case I: u_g at $t = 1s$



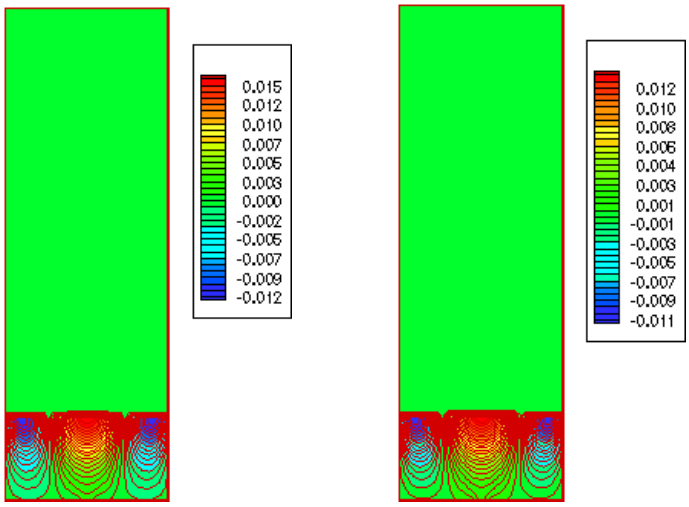
(a) MFIX (b) ODExS

Figure 53: Case I: v_g at $t = 1s$



(a) MFIX (b) ODExS

Figure 54: Case I: u_s at $t = 1s$



(a) MFIX (b) ODExS

Figure 55: Case I: v_s at $t = 1s$

combining the numerical results of MFIX obtained for three different values of D_p: 0.05, 0.07 and 0.10 cm. For every solids particle diameter, 320 snapshots were calculated using MFIX. The database was generated by combining the snapshots of these three conditions. Thus, 960 snapshots were included in the database. The PODDEC package was applied to this database to extract the POD basis functions. Using these POD basis functions, the reduced order model ODExS was generated and used to simulate the transport phenomena in case I at 13 different values of D_p. The number of POD basis functions was $m^{p_g} = 2$, $m^{u_g} = 15$, $m^{v_g} = 11$, $m^{u_s} = 10$, and $m^{v_s} = 5$ such that the reduced order model captured 99.99% of the total energy.

Table 8 lists the errors of the field variables obtained from ODExS compared against the numerical results of MFIX at $t = 1s$. These errors are also shown in Figure 56. As seen from Table 8 and Figure 56, ODExS provided good predictions of the field variables for $D_p \in [0.05\ cm, 0.10\ cm]$. For D_p values outside of the $(0.05\ cm, 0.10\ cm)$ interval, the error increased rapidly, especially for $D_p < 0.05\ cm$ where the physics of the transport phenomena had significantly changed. Figure 57 shows the contour plots of the gas void fraction ϵ_g at $t = 1s$ obtained using MFIX for three values of D_p : 0.03, 0.08 and 0.12 cm. At $D_p = 0.03\ cm$, bubbles appeared in the lower central part of the bed. Since no basis functions were generated for the bubbling fluidization regime, the errors of the reduced order model were higher for $D_p < 0.05\ cm$ than for the other values of D_p where no bubbling fluidization was present. To improve the prediction of the reduced order model, snapshots of the solution corresponding to solid particle diameter $D_p < 0.5\ cm$ need to be used too when the basis functions are generated.

Table 8: Case I: ODExS errors at off-reference conditions

D_p [cm]	ϵ_{ϵ_g} [%]	ϵ_{p_g} [%]	ϵ_{u_g} [%]	ϵ_{v_g} [%]	ϵ_{u_s} [%]	ϵ_{v_s} [%]
0.03	0.0733	0.00051	9.71	2.41	8.61	9.09
0.04	0.0137	0.000077	2.495	0.389	10.45	4.713
0.05	0.00186	0.0000022	0.0686	0.0517	1.08	3.18
0.055	0.00158	0.00000272	0.102	0.044	1.08	2.967
0.06	0.00136	0.0000045	0.166	0.0494	1.57	2.73
0.07	0.00100	0.0000044	0.191	0.0578	1.52	2.16
0.08	0.00073	0.0000024	0.122	0.0423	0.679	1.50
0.09	0.00054	0.00000027	0.0298	0.0235	0.766	0.807
0.10	0.00042	0.00000027	0.161	0.0191	2.29	0.194
0.11	0.000376	0.0000051	0.323	0.0524	3.917	0.841
0.12	0.000368	0.0000072	0.487	0.1005	5.53	1.75
0.13	0.000374	0.0000091	0.654	0.129	7.56	2.711
0.14	0.000451	0.0000107	0.819	0.191	9.128	3.736

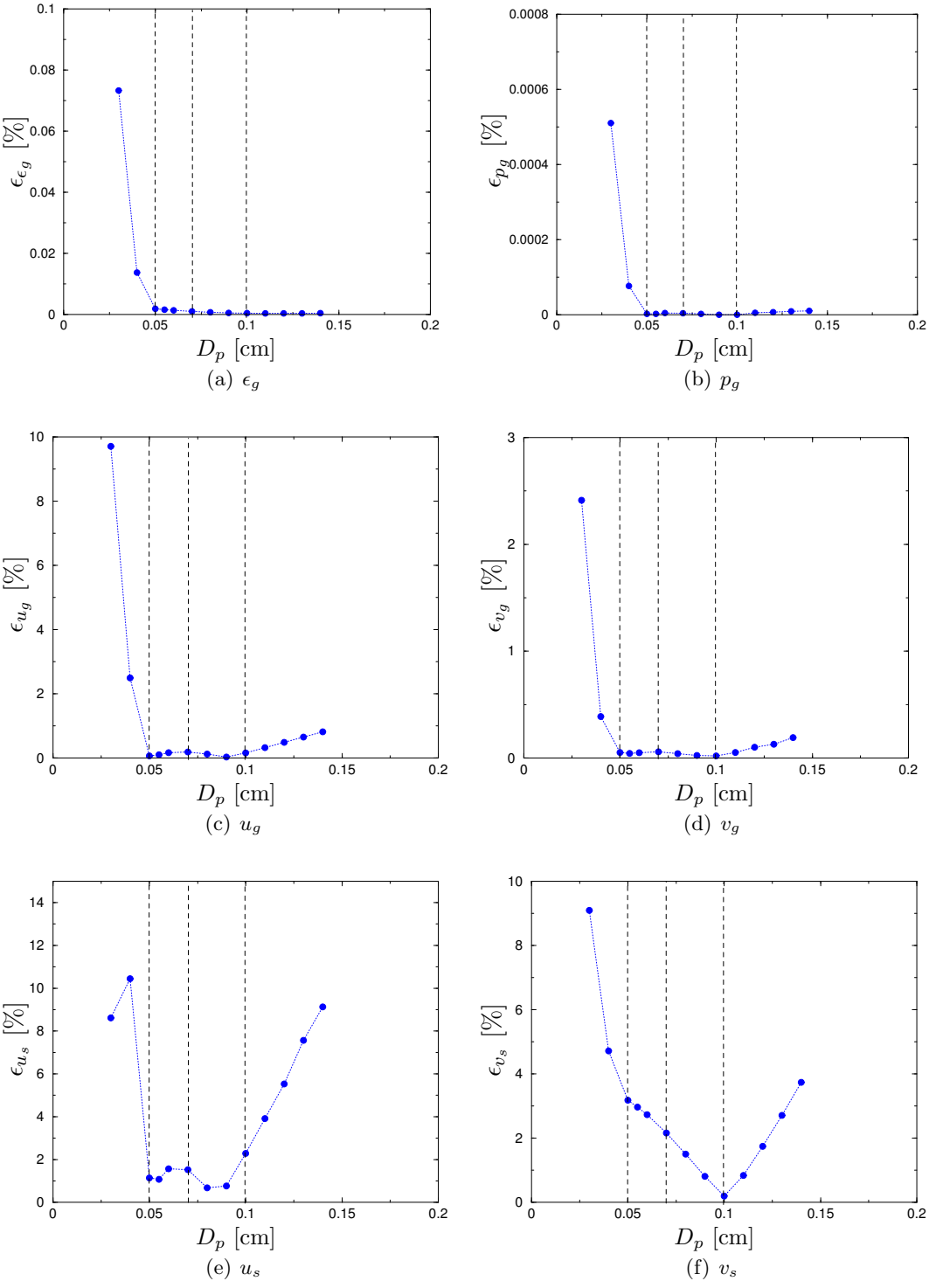
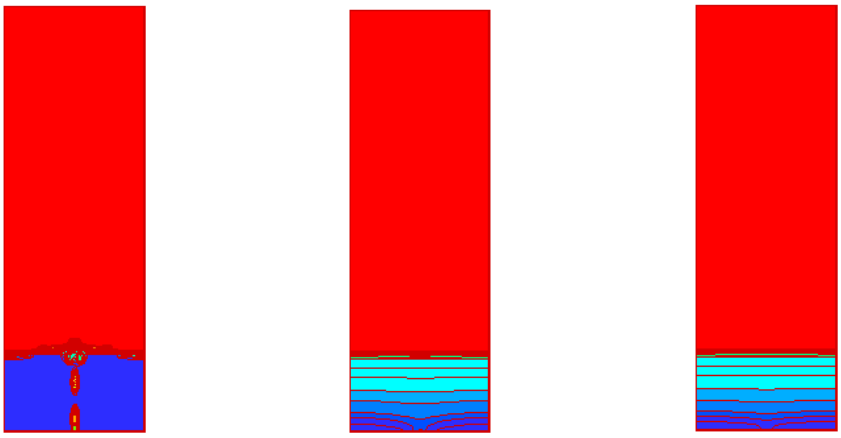


Figure 56: Case I: ODExS errors at off-reference conditions



(a) $D_p = 0.03cm$ (b) $D_p = 0.08cm$ (c) $D_p = 0.12cm$

Figure 57: Case I: contour plots of ϵ_g at $t = 1s$ and different D_p

4.5 Visualization tools for Galerkin ODEs

The work on the visualization tools for Galerkin ODEs included writing code to visualize POD-reconstructed flow motion, and animation of the temporal evolution of the flow in phase space through POD time coefficients. These tasks were accomplished aided by the POD spatial modes and their amplitude coefficients, which were extracted from numerical simulations via MFIX.

Various visualization tools demonstrating the results of the POD decomposition have been created. These tools include: animations of reconstructed flow with increasing number of POD modes, phase-space animations depicting the temporal evolution of POD time-dependent coefficients, combined animations of the space-time evolution of the flow together with a track along the time-dependent coefficients, and 3D animations of successive POD reconstructions.

Fine-tunning of visualization tools, via comparisons between POD animations, original MFIX simulations, and reconstructions with reduced ODEs, has been completed. Longer MFIX simulations, *i.e.*, up to 20 seconds or 2000 frames, have also been completed.

5 Conclusions

The project developed a reduced order model for transport phenomena in fluidized beds. Several algorithms have been implemented and tested against the full model (MFIX). The reduced order models were developed first for gas-only flows. The reduced order models were subsequently developed for gas and solids transport phenomena. These reduced order models did not include the energy balance equations. The reduced order model included only one solids phase.

The reduction of computational time obtained by using the reduced order model vs. the full model depended on the total energy captured by the POD modes. The total energy captured by the POD modes increased with the number of POD modes. The accuracy of the reduced order model increased as the number of POD modes increased. Consequently, a higher accuracy of the reduced order model required a higher computational cost. For the cases investigated, it was found that when the energy captured by the POD modes was 99.99% of the total energy, the accuracy of the reduced order model was excellent, as shown in Table 7. For this case, the computational time of the reduced order model compared to the full model was reduced to approximatively one third.

Higher computational speed-ups were obtained when the energy captured by the POD modes decreased. The complexity of the transport phenomena in the fluidized bed required that at least 99% of the total energy be captured by the POD modes in order to obtain acceptable accuracy. For a reduced order model where the POD modes cover 99% of the total energy, the computational time of the reduced order model was more than 10 times smaller than the computational time of the full model.

Further work is needed in order to improve the reduced order model. The reduced order model should be extended to include the energy equation. The reduced order model should also be extended from two-dimensional to three-dimensional problems. To further reduce the computational cost of the reduced order model, a parallelized algorithm should also be developed and implemented.

References

[1] P. G. A. Cizmas, A. Palacios, T. O'Brien, and M. Syamlal. Proper-orthogonal decomposition of spatio-temporal patterns in fluidized beds. *Chemical Engineering Science*, 58(19):4417–4427, October 2003.

[2] D. Gidaspow. *Multiphase Flow and Fluidization.* Academic Press, Boston, 1994.

[3] M. Syamlal. MFIX documentation numerical technique. Technical Report DE-AC21-95MC31346, EG&G Technical Services of West Virginia, 1998.

A SAMPLE INPUT FILE FOR ODExMFIX

```
#
# odexmfix.dat
# ODExMFIX input file for case I
# 1.1 Run control section
#
  TSTART  = 0.02
  TSTOP   = 5.0
  DT      = 1.D-3
  MAX_NIT = 20
  DT_MAX  = 1.D0
  DT_MIN  = 1.D-6
  DT_FAC  = 0.9D0
  TOL_RESID = 1.D-3
  TOL_DIVERGE = 1.D+2
#
# 1.2 Geometry and discretization section
#
  XLENGTH = 25.4D0     IMAX = 50
  YLENGTH = 76.5D0     JMAX = 76
  DISCRETIZE = 2
#
# 1.3 physical properties section
#
  MU_g0 = 1.8D-2
  MW_g0 = 29.D0
  T_g0  = 297.D0
#
# 1.4 pod section
#
   NP = 3
   NU = 7
   NV = 5
```

B SAMPLE INPUT FILE FOR ODEx3

```
#
# ODEx3 input file for case II
#
# 1.1 Run control section
#
  TIME  = 0.2
  TSTOP = 13.0
  DT    = 1.D-5
  ATOL  = 1.D-3
#
# 1.2 Geometry and discretization section
#
  XLENGTH = 25.4D0     IMAX = 50
  YLENGTH = 76.5D0     JMAX = 76
  DISCRETIZE = 1
#
# 1.3 physical properties section
#
  MU_g0 = 1.8D-4
  MW_g0 = 29.D0
  T_g0  = 297.D0
#
# 1.4 pod section
#
   NR = 9
   NU = 11
   NV = 7
```

C SAMPLE INPUT FILE FOR ODExS

```
#
# Hybrid_puv input file for case II
#
# 1.1 Run control section
#
  TSTART  = 0.20
  TSTOP = 1.0
  DT    = 2.D-4
  MAX_NIT = 20
  DT_MAX  = 1.D0
  DT_MIN  = 1.D-6
  DT_FAC  = 0.9D0
  TOL_RESID = 1.D-3
  TOL_DIVERGE = 1.D1
#
# 1.2 Geometry and discretization section
#
  XLENGTH = 25.4D0     IMAX = 50
  YLENGTH = 76.5D0     JMAX = 78
  DISCRETIZE = 2
#
# 1.3 physical properties section
#
  MU_g0   = 1.8D-4
  MW_g0   = 29.D0
  T_g0    = 297.D0
  RO_s0   = 1.0
  D_p     = 0.05
  C_e     = 0.8
  Phi     = 30.0
  EP_star = 0.44
#
# 1.4 POD section
#
  nP_g    = 4
  nU_g    = 11
  nV_g    = 7
  nU_s    = 7
  nV_s    = 5
```